NTNU
Norwegian University of
Science and Technology

Design and Hydrodynamic Analysis of a Semi-submersible with Two 5WM Wind Turbines

Peng Ai

Maritime Engineering
Submission date: June 2016
Supervisor: Zhen Gao, IMT

Norwegian University of Science and Technology
Department of Marine Technology

Design and hydrodynamic analysis of a semi-submersible floater supporting two 5MW wind turbines

Peng Ai

May 2016

Nordic Master of Science in Maritime Engineering

MASTER THESIS

Norwegian University of Science and Technology

Department of Marine Technology

KTH Royal Institute of Technology

Department of Aeronautical and Vehicle Engineering

Supervisor 1: Professor Zhen Gao, NTNU

Supervisor 2: Professor Karl Garme, KTH

Preface

This thesis is written as the final part of my master study of Maritime Engineering(offshore structure track) from both Royal Institute of Technology and Norwegian University of Science and Technology between 15^{th}, January, 2016 and 15^{th}, June, 2016.

The multiple turbine idea was initially influenced by a Swedish company Hexicon. The fundamental interests in the thesis are to examine the response behavior of the floater with two turbines so that the response behavior can be studied and the most vulnerable degrees of freedom can be determined for this type of turbine.

It was a true learning experience and I had fun looking into different components in the rigid body dynamic motion equations and trying to solve them from a simple model to more comprehensive models.

I hope this work will possibly inspire some on the response analysis of semi-submersible floaters, especially when more than one turbines are present.

Trondheim, 2016-06-10

Peng Ai

Acknowledgment

First of all, I would like to thank the coordinators of Nordic Master Maritime Engineering program, Poul Andersen, Anders Rosén and Svein Sævik. This thesis would be impossible without joining this exciting program.

Heartfelt thanks for Prof. Zhen Gao at NTNU for inspiring and patient academic guidance and Dr. Karl Garme for critical comments and feedback on the study during the process of the thesis.

I also benefit a lot from the discussions with PhD candidates Chenyu Luan regarding the initial design of the floater. Besides, PhD candidate Ling Wan and Dr. Xiaopeng Wu helped me with simulation tool SIMA and TDHMILL.

I truly appreciate all my friends around me at Poolen, KTH and Tyholt, NTNU for the amazing time we had together!

Last but not the least, I would like to thank my caring parents for their support, encouragement and love!

Peng Ai

Summary and Conclusions

Offshore wind energy has been experiencing a rapid development for last decade. High cost is still the main challenge for the offshore wind industry. Additionally, bottom fixed floating wind turbines may become costly for water depth larger than 50m. An effective way to reduce the cost could be to increase the amount of power generation by a single turbine structure.

In this thesis, a semi-submersible platform has been designed to support two NREL 5MW wind turbines, whose cost is possibly decreased through a more effective utilization of the floater structure and mooring system and other auxiliary devices. The design is then checked against buoyancy, stability criteria. First order and second order hydrodynamics are analyzed.

In addition to the floater, a mooring system has been designed based on the catenary theory. Spectrum analysis of the mooring line tension has been performed to identify the eigenfrequencies of the moored structure.

In the hydrodynamic analysis, floating wind turbine models with different levels of complexity have been established and studied through the thesis. Viscous drag forces and second order wave forces have also been implemented.

Finally a simplified time domain method to include the aerodynamic forces are proposed. Unfortunately, a mismatch of the software has not solved within the time limit. High chances are the aerodynamic forces can be simulated to an acceptable accuracy for response analysis by the proposed method.

Contents

CHAPTER 1

Introduction

1.1 Development

Offshore wind industry is relatively young compared to other established offshore industries like shipping and oil&gas. The first commercial offshore wind farm was proposed and invested at Denmark in 1991. Since 2001, offshore wind industry has been experiencing drastic growth and has developed into one of the key renewable energy industries in EU. A tremendous growth of the industry can be seen in Figure 1.1

A current offshore wind target worldwide is described in the Eon's annual report [4]. Offshore wind energy in Europe is supposed to grow strongly over the next decades.

- North America targets for 3,000 WM before 2020
- EU targets for 40,000 WM before 2020
- China targets for 6,000 WM before 2020
- South Korea targets for 2,500 WM before 2020

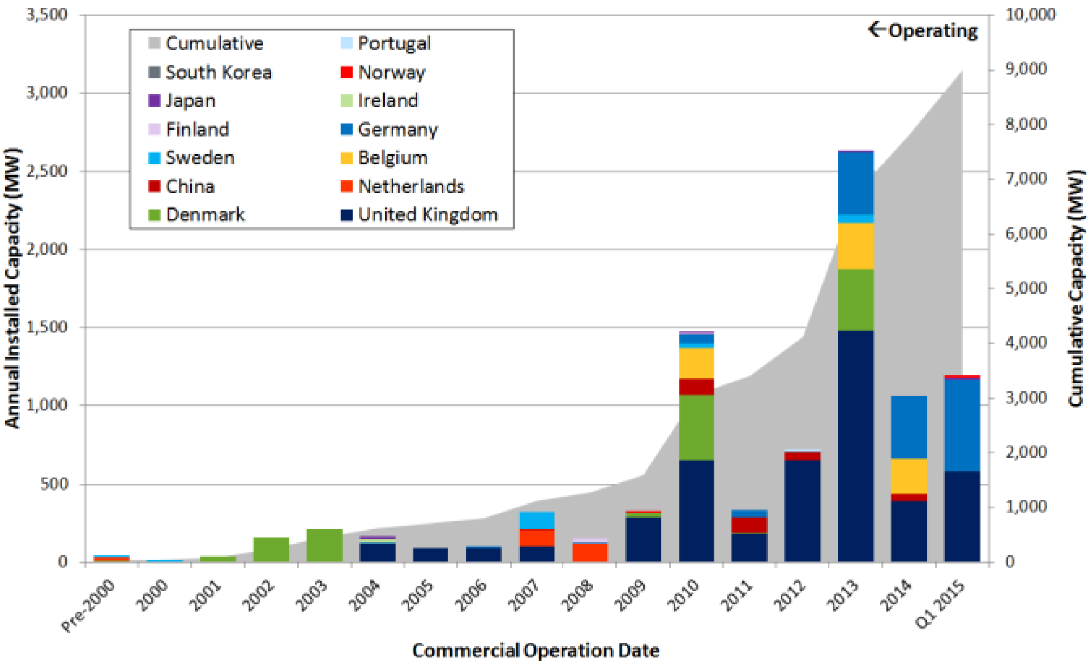

Figure 1.1: Operating global offshore wind capacity (annual and cumulative) [11]

1.2 Pros and Cons for Offshore Wind Turbines

Onshore wind turbines have been developed much earlier than offshore wind turbine. The main differences between onshore and offshore wind energy is collected below.

Offshore wind energy has much greater potential but rougher marine conditions, which is the main reason of the recent shift from onshore to offshore. On the other hand, offshore wind turbines pose much more challenges technically and economically, not only the robustness of the structures but also the stable power output under a complex combination of wind and waves.

1.3 Trends

It is reported by the American National Renewable Energy Laboratory that until September, 2015, monopiles have been the dominant substructure historically with a 75% market share[11]. A growing market share from jackets is also expected as the industry moves to deeper water.

Floating substructures, on the other hand, show a potential to make a significant contribu-

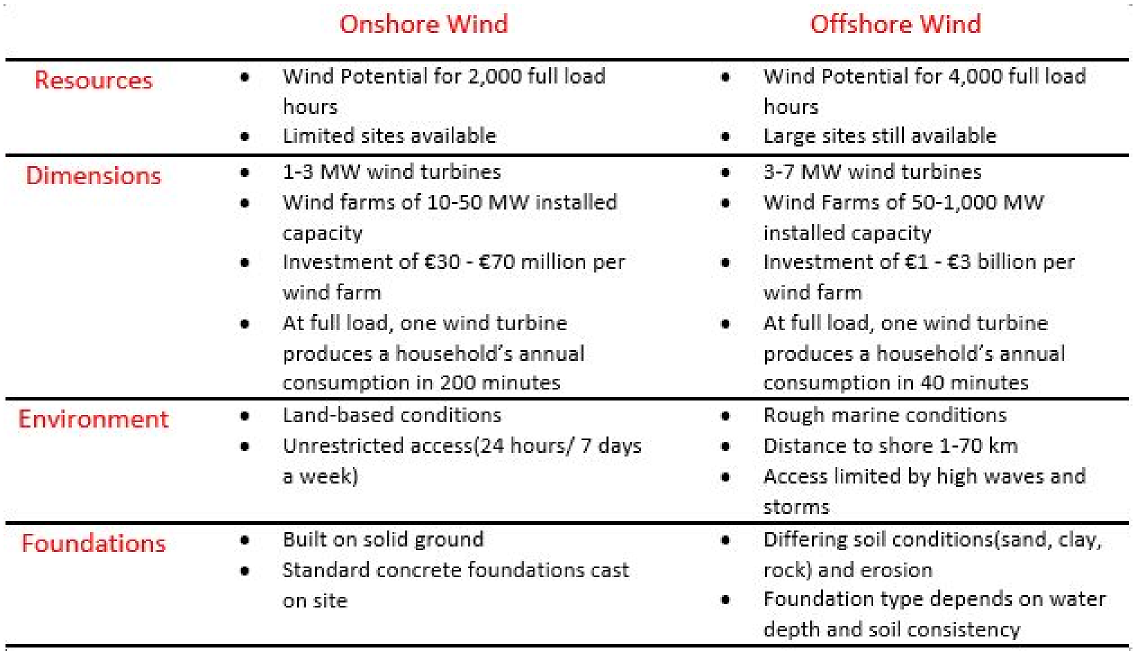

	Onshore Wind	Offshore Wind
Resources	- Wind Potential for 2,000 full load hours - Limited sites available	- Wind Potential for 4,000 full load hours - Large sites still available
Dimensions	- 1-3 MW wind turbines - Wind farms of 10-50 MW installed capacity - Investment of €30 - €70 million per wind farm - At full load, one wind turbine produces a household's annual consumption in 200 minutes	- 3-7 MW wind turbines - Wind Farms of 50-1,000 MW installed capacity - Investment of €1 - €3 billion per wind farm - At full load, one wind turbine produces a household's annual consumption in 40 minutes
Environment	- Land-based conditions - Unrestricted access(24 hours/ 7 days a week)	- Rough marine conditions - Distance to shore 1-70 km - Access limited by high waves and storms
Foundations	- Built on solid ground - Standard concrete foundations cast on site	- Differing soil conditions(sand, clay, rock) and erosion - Foundation type depends on water depth and soil consistency

Figure 1.2: Comparison between Onshore Wind and Offshore Wind
[6]

tion to the global market. The American National Renewable Energy Laboratory provides the data of wind projects as a function of water depth[11]. Figure 1.3a clearly reveals a deep water trend in the industry.

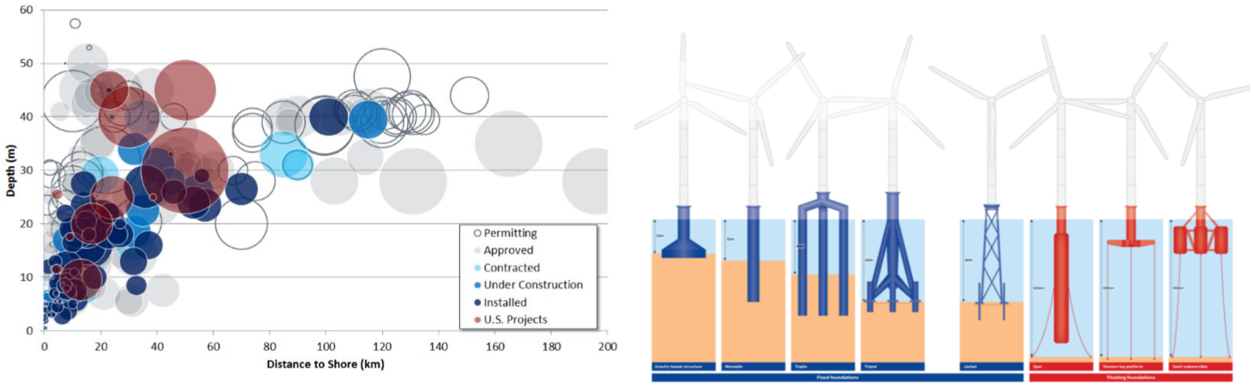

(a) Global offshore wind projects as a Function of water depth and distance to shore

(b) Various floater types

Figure 1.3

1.4 Innovative Design

The water depth of 50m is critical. According to European Wind Energy Association[6], current commercial substructures of offshore wind turbines, such as gravity, jacket, monopile, are economically limited around maximum water depths at 40-50m because the size of the floater. Afterwards starts the deep water environment where new offshore concepts must be developed in order to take advantage of the larger wind potential in Atlantic Ocean, Mediterranean Sea and North Sea.

Many floating concepts have already been proposed, as demonstrated in Fig 1.3b. The three dominant floating typologies for floating wind turbines(spar, semi-submersible and TLP), along with their associated components(e.g. mooring, anchors), are mainly inherited from oil&gas industry. However, oil&gas industry is different from offshore wind industry because the structures are made for distinctive needs. Rhodri James[33] also examined numerous existing floating wind concepts and concluded that “in all likelihood there will not be a single wining concept, but a range of leading devices suitable for different site contains an overview of the various concepts currently under development which are vying for market leader position in the race to commercialize their designs”.

1.5 Multiple Unit Offshore Wind Turbines

Inspired by oil&gas industry, the prototypes of bottom-fixed or floating turbines have long been establish. However, unlike the oil&gas industry, a good solution of floating turbine concepts for offshore wind utilization could be the multiple wind turbines installed on one floater.

It is widely accepted that the cost increase of offshore wind turbines are not very sensitive to their size increase. Therefore, if the infrastructure is properly developed, an offshore floater with multiple wind turbines would possess a very plausible commercial advantage for all the stakeholders in the offshore wind power industry.

Quite a few multiple unit offshore wind turbine concepts have already been developed in the design phase and the interests in the multiple turbine arrangements are increasing. After viewing many concepts, five promising concepts among them are introduced here.

1. **Hexicon**(Sweden) [7].

   Hexicon has gone through different plans and the latest plan shows in the Figure 1.4, consisting of a series of buoyancy columns distributed triangularly in a large truss structure. Three wind turbines are aligned on one side of the platform. The structure is catenary moored both for stability and keep the platform to the wind direction. The flexibility to turn the platform ensure the platform to be adjusted for the best wind direction. The general design information of Hexicon is collected in Table 1.1

Figure 1.4: Hexicon design

Table 1.1: Design information of Hexicon

Material	Steel	Moorings	8 catenary
Depth Range	50-500 m	Size	$464m \times 77m$
Hub Height	105m	No. blades	3

2. **WindSea**(Norway) [10]

   WindSea is a semi-submersible floater with multiple turbines. Three outriggers connected to the main structure, which mainly consists of three vertical columns, a ring pontoon at the bottom and box girders at the top. Three turbines do not face at the same direction; two upwind and one downwind. The design is demonstrated in Figure 1.5.

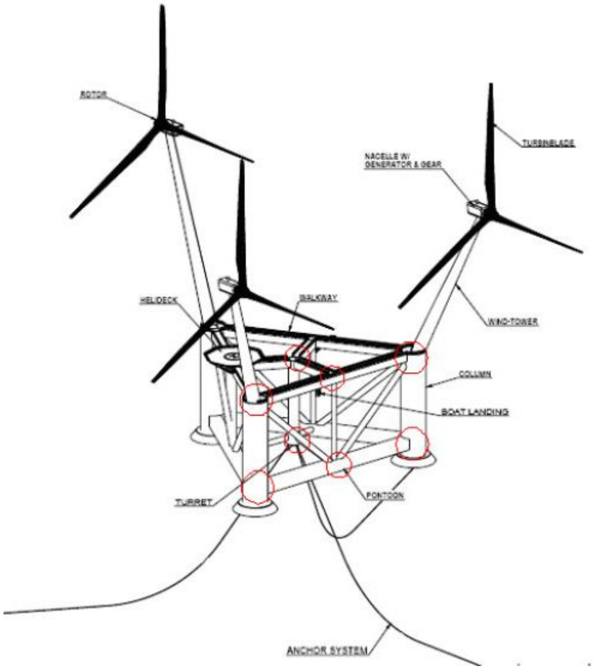

Figure 1.5: WindSea

The designers claim such inclined towers help to minimize wake looses. Red circles below shows hot spots on the structure. The general design information of Hexicon is collected in Table 1.2

Table 1.2: Design information of Windsea

Material	Steel	Moorings	3 catenary
Depth Range	50-120 m	No. blades	3
Hub Height upwind	71m	Hub Height downwind	90m

3. **W2Power**(Norway) [9]

W2Power is a hybrid wind & wave energy plant where "two corners of the triangle support one wind turbine each and the third corner houses the power take-off for the wave energy conversion system. Figure 1.6 shows the concept. The wave energy device uses a conventional Pelton turbine driven by three lines of wave-actuated hydraulic pumps mounted on the platform's sides."[9] The whole platform is estimated to reach a total unit capacity of up to 10WM in areas with strong waves, given two 3.6 MW standard offshore wind turbines e.g. the Siemens 3.6-107 turbines. Table 1.3 gives a rough design information.

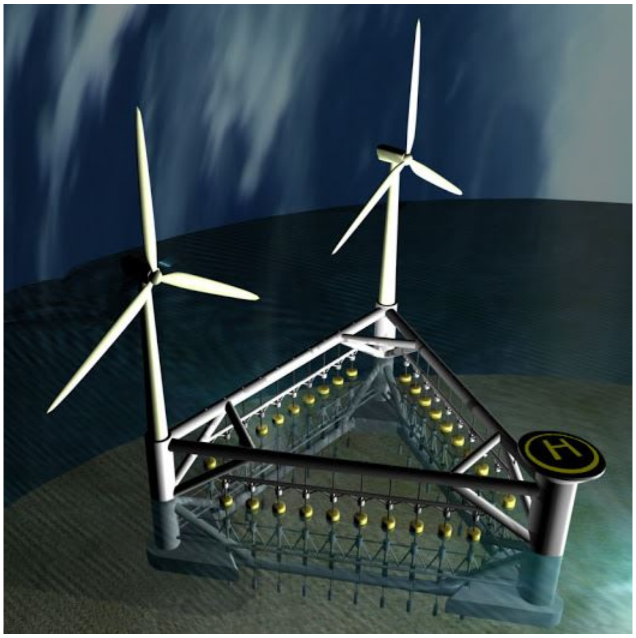

Figure 1.6: W2Power

Table 1.3: Design information of W2Power

Material	Steel	Moorings	Undisclosed
Depth Range	Undisclosed	No. blades	3
Hub Height	80-85m	Size	Undisclosed

4. **Poseidon**(Denmark) [8]

   Poseidon has two plans, of which P37 is the multiple turbines concept. P37 has three turbines triangularly posed on a floater with 10 wave power units, rated at 400-650 kWh each. A turret mooring system is adopted, allowing a passive rotation up to 260 degrees to face the incoming waves. A 1 : 2.3 scale structure P37 was installed in 2010, supporting 3 turbines with a total capacity of 0.03 MW[33].

Table 1.4: Design information of Poseidon P37

Material	Steel	Moorings	Undisclosed
Depth Range	Undisclosed	No. blades	3
Weight	320 t	Size	$25m \times 37m$

5. **WindLens**(Japan)

   WindLens are semi-submersible multi-turbine platform consisting of a series of hexagonal platforms, on each of which two WindLens turbines are installed and the rest of available area is covered in solar PV panels.

Table 1.5: Design information of WindLens

Material	Steel	Moorings	Undisclosed
Depth Range	Undisclosed	No. blades	3
Weight	Undisclosed	Size	Undisclosed

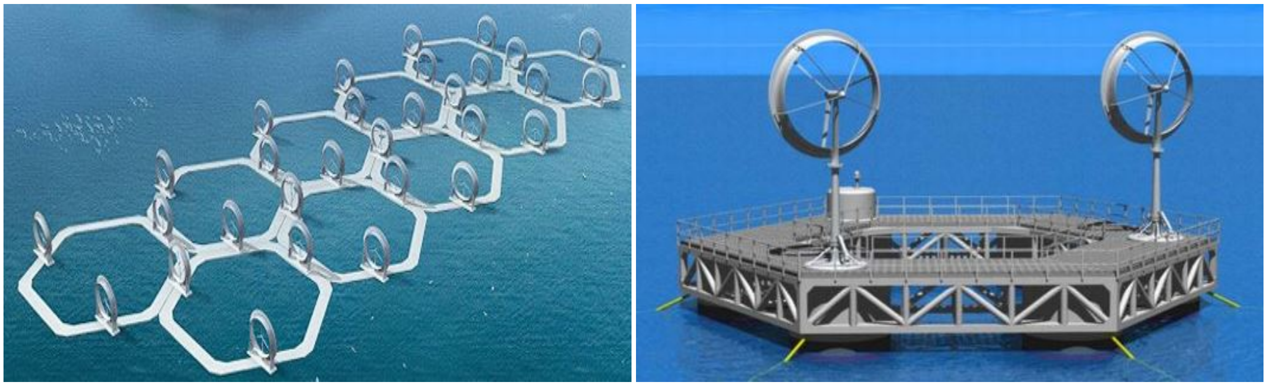

(a) WindLens assembled plan

(b) WindLens single plan

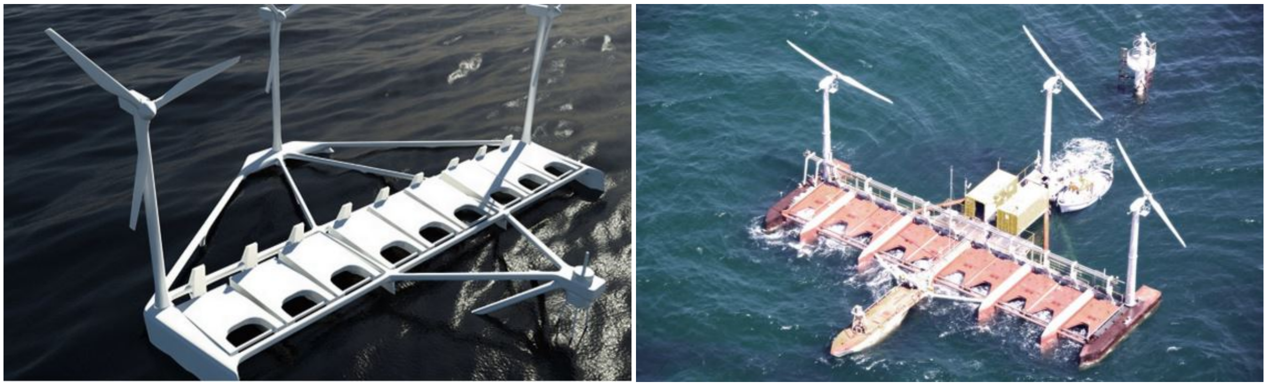

(c) Poseidon P37 Design Sketch

(d) Poseidon P37 Scale model

Figure 1.7

From all of the concepts listed above, it is clear that the designers tend to maximize the power output from one floater. Due to a large deck area, floater of multiple wind turbines can hold either wave energy conversion system or solar panels to further boost generated power.

Especially, Anders Yde et al.[13] reported interesting experimental results of Poseidon P37.

The hydrodynamic characteristics of the platform was quite stable and it survived the storm on $October \quad 28^{th}$,2013, demonstrating an outstanding stability.

1.6 Scope of the Thesis

The aim of this thesis is to study the response behavior of the floater supporting two 5MW wind turbines, subjected to aerodynamic and hydrodynamic loads. Before the response analysis, a simple design of the platform structure and mooring system is also performed.

The analysis of the turbine is performed with different level of complexity:

1. the frequency domain first order hydrodynamic analysis without mooring system.
2. the frequency domain second order hydrodynamic analysis without mooring system.
3. the time domain hydrodynamic analysis with mooring system.
4. the time domain hydrodynamic&aerodynamic analysis with mooring system.

Due to the amount of the work and limited time, the focus of the thesis is primarily put on the dynamic analysis of the structure. Structural strength and fatigue damage of the structure is neglected.

Unfortunately, the aerodynamic loads results are not presented. A possible way to include the aerodynamic loads from two turbines is discussed in section 8.2. But a mismatch of the software version happened, which could have been solved given more time.

CHAPTER 2

Fundamental Theory

Wind turbines are complex systems subject to wind and wave loads, therefore the analysis includes both hydrodynamics and aerodynamics. Considerations of structural robustness could should have been considered, but the focus of the study is on the motion responses of the platform. Structural mechanics of the design is hence excluded.

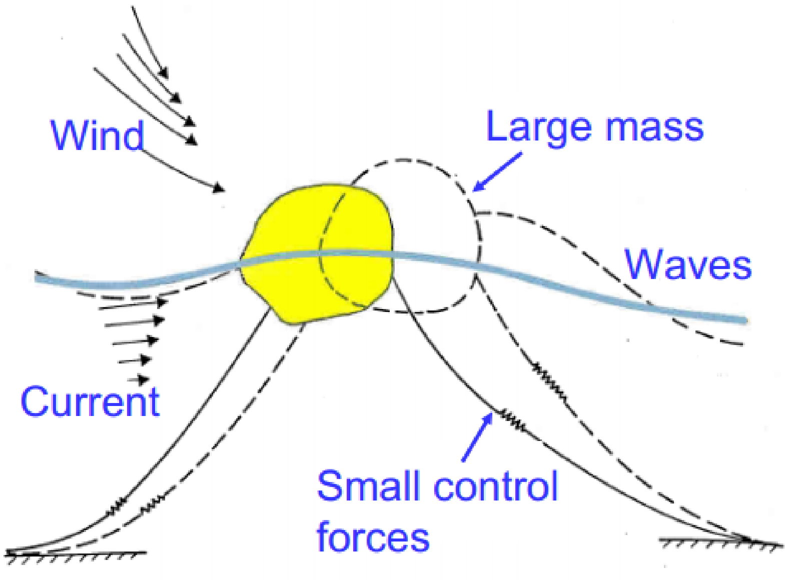

Figure 2.1: Simplified Physical Model for a Semi-submersible

Over a lifetime, an offshore wind turbine could be exposed to various load conditions, from environment(wind, wave, current and ice), from its operation(installation, startup, shutdown, normal operation, parked and faulted) and from accident(collision, ballast system failure, loss of mooring lines, fire etc.) During this study, only the normal operation condition is considered as the primary load condition during the analysis.

Considering an offshore wind turbine as a rigid body, as figure 2.1, the forces the platform is subject to include wind loads, wave loads, current and mooring system. To understand the motion under such a multidisciplinary environment, relevant theoretical background information is given:

1. Descriptions of waves and winds
2. Turbine hydrodynamics
3. Turbine aerodynamics
4. Wave and wind coupled dynamics

2.1 Random Environmental Processes

A brief description of both are presented, before determining the site conditions where the turbines are simulated. Mathematical definition of a stochastic process is not of interest of the study. For this semi-submersible wind turbine, two random environmental processes are of particular interest: wave elevation and wind speed.

2.1.1 Waves and Wave spectrum

Waves and loads are stochastic processes. Driven by wind, waves are travelling in different directions with strong non-linearity and the viscosity is notable. Fortunately, linear potential flow theory is a reasonable for this complicated situation. It assumes a incompressible, irrotational and inviscid flow. [19]

Following linear potential theory, irregular seas can be expressed as a sum of regular wave components with different frequencies. Equation (2.1) gives a mathematical expression of the free surface elevation for long-crested waves travelling in positive x-direction.

$$\zeta(t) = \sum_{i=1}^{N} A_i sin(\omega_i t - k_i x + \epsilon_i) \tag{2.1}$$

where A_i is the wave amplitude, ω_i is the frequency, k_i is the wave number and ϵ_i is the phase angle of the i^{th} regular wave component. Depending on the water depth, ω_i and k_i are governed by the dispersion relation.

Practically, these wave components are often described by the wave spectrum, S_w. Diving the spectrum into i components in frequency domain with constant spacing $\Delta\omega$ and ϵ_i is a uniformly distributed variable over the interval $[0,2\pi]$, the amplitude A_i can be expressed mathematically as,

$$\frac{1}{2}A_i^2 = S_w(\omega_i)\Delta\omega \tag{2.2}$$

Equation 2.2 has been used to obtain the wave elevation in the thesis.

There are several numerical approximations of wave spectra based on known wave data: JONSWAP, ISSC and Pierson-Moskowitz spectra. These spectra describe wind-generated waves. In North Sea conditions, the most applicable one is JONSWAP spectrum[24].

$$S_w(\omega) = \frac{\alpha g^2}{\omega^5} \exp\Big(-\beta\Big(\frac{\omega_p}{\omega}\Big)^4\Big)\gamma^{a(\omega)} \tag{2.3}$$

where

$$a(\omega) = \exp\frac{(\omega/\omega_p - 1)^2}{2\tilde{\sigma}^2} \tag{2.4}$$

and

$$\tilde{\sigma} = \begin{cases} 0.07, \omega \leq \omega_p \\ 0.09, \omega \geq \omega_p \end{cases} \tag{2.5}$$

α is a spectral parameter, β is the form parameter and γ is the peakedness parameter.

Two important parameters to describe the wave environment are the significant wave height, H_s, and the peak period, T_p. By definition, H_s is the mean value of the one-third largest waves and T_p is the period at which the spectrum takes on its largest value. In the JONSWAP spectrum, H_s can be related to the spectral parameter α in Eq 2.3, and $T_p = \frac{2\pi}{\omega_p}$.

2.1.2 Wind and Wind Spectrum

Wind is another stochastic sources of the turbine excitation loads. The wind speeds are usually modelled as a three dimensional velocity field of longitudinal, later and vertical components, where the longitudinal component is taken along the primary wind direction.

The mean wind speed is typically reported for periods of 10 minutes or 1 hour. Then, the longitudinal wind speed U at a particular point in space is generally described as the sum of mean and fluctuating parts:

$$U = \bar{U} + u' \tag{2.6}$$

where $\bar{U}$ is the short-term mean wind speed and u' is a fluctuating component. Similarly, the lateral and vertical wind speeds consist of mean and fluctuating components. In this study, the lateral and vertical wind speeds are assumed to be zero.

Important temporal variations occurs in wind speed across a wide range of time scales: inter-annual, annual, diurnal and short-term. Turbulence intensity I is defined as the ratio between the mean wind speed at a reference height and the standard deviation of the wind speed. I generally varies from approximately 0.1 to 0.4 and tends to be larger for lower wind speed.

$$I = \frac{\sigma_u}{\bar{U}} \tag{2.7}$$

Normally, the turbulence intensity can be obtained from design standards [20].

Additionally, there is a significant variation of the mean wind speed as the height changes. In this study, the power law formulation is applied to describe this mean longitudinal wind speed change as a function of height,

$$\bar{U}(z) = \bar{U}_{ref}\left(\frac{z}{z_{ref}}\right)^{\alpha} \tag{2.8}$$

where α is the power law exponent. For offshore locations, α is recommended to be 0.14

Kaimal spectrum is used as the dynamic wind spectrum in the study. It is given as,

$$S_{Kaimal}(f) = 4\sigma_u^2 \cdot \frac{L_k}{\bar{U}} \cdot \frac{1}{\left(1+6f\frac{L_k}{\bar{U}}\right)^{\frac{5}{3}}} \tag{2.9}$$

where

$\sigma_u = I \cdot (\bar{U} \cdot 0.75 + 5.6)$

$L_k = 8.1 \cdot \lambda$, λ is a spectral parameter

In the absence of detailed wind observations for a particular location, the turbulence intensity can be obtained from design standards. The IEC standard proposes a normal turbulence model (NTM) and an extreme turbulence model (ETM) [5]. In the present thesis, the NTM and ETM models were applied for IEC Class B and C.

2.2 Semi-submersible Hydrodynamics

Hydrodynamic loads may include waves, current, tidal variations for any kind of offshore structures. The thesis focus mainly on wave loads due to a deep water site condition.

For large volume offshore structures, for example the designed turbine, first order potential flow theory gives a good estimation for the added mass, radiation damping coefficients and wave excitation. First order potential flow theory considers the excitation at the incoming wave frequency and the responses are oscillating about the equilibrium position.

Second order potential flow theory becomes important when the natural frequencies of the structure are either quite low or high because second order forces consist of mean drift terms, sum-frequency terms and difference-frequency terms. For semi-submersibles, the second order forces are important for all the 6 degrees of freedom because eigenfrequency at each DOF is low for a semi-submersible.

For any slender structures in water, hydrodynamic forces might be estimated by Morison Equation, which is a semi-empirical formulation for inertia and viscous drag loads. This equation is used in calculation because the structure consists of columns and braces.

2.2.1 First Order Potential Flow Theory

The wave-frequency motion is mainly linearly-excited motion in the frequency domain. First order potential flow theory is quite sufficient to describe the major wave loadings on offshore structures.

A velocity potential has no physical meaning and it is introduced due to the mathematical analysis of irrotational fluid motion. By definition, instantaneous speed V and the velocity potential ϕ has the relation as below,

$$\mathbf{V} = \bigtriangledown\phi = \frac{\partial\phi}{\partial x}\mathbf{i} + \frac{\partial\phi}{\partial y}\mathbf{j} + \frac{\partial\phi}{\partial z}\mathbf{k} \tag{2.10}$$

where **V** denotes the flow velocity. ϕ is the velocity potential. **i**, **j** and **k** are unit vectors along the $x-, y-, z-$ axes.

If a steady flow condition is assumed, which means the properties of the fluid, such as pressure and velocity, is independent of time and is only a function of space (x, y, z). Under this situation, the space and time variables in $\phi(x, y, z, t)$ can be separated and Laplace equation and its boundary conditions can be satisfied mathematically, by assuming the velocity potential in the form as,

$$\phi = \varphi(x, y, z)T(t) \tag{2.11}$$

For waves with a generic direction β with respect to x, the incident wave velocity potential becomes,

$$\phi^{(1)} = \frac{\zeta_a g}{\omega_0} e^{kz} cos(\omega_e t - kxcos\beta - kysin\beta) \tag{2.12}$$

where k is the wave number and (x, y, z) is spatial coordinate. ω_0 is the wave frequency while as ω_e is the encounter frequency. It is seen that the wave incident angle β will introduce a phase shift and that the velocity potential is proportional to the wave amplitude ζ_a.

The solution of the first order velocity potential gives the frequency-dependent added mass, linear damping and wave excitation. These parameters will be further required to solve the first order motion responses.

2.2.2 Second Order Potential Flow Theory

The second order velocity potential, in comparison to the first order, is expanded as,

$$\phi(x,t) = \epsilon\phi^{(1)}(x,t) + \epsilon^2\phi^{(2)}(x,t) \tag{2.13}$$

$\phi^{(2)}(x,t)$ is resulted from the interaction between two waves. For a plane waves with frequency ω_i and ω_j, the second-order potential $\phi^{(2)}$ includes both difference-frequency and sum frequency components,

$$\phi^{(2)}(x,t) = Re\sum_i\sum_j\left[\phi_{ij}^{+}(x)e^{i(\omega_i+\omega_j)t} + \phi_{ij}^{-}(x)e^{i(\omega_i-\omega_j)t}\right] \tag{2.14}$$

These two components ϕ_{ij}^{+} and ϕ_{ij}^{-} are typically solved separately. Slow varying forces, which could be important for a semi-submersible, are obtained by integrating the difference frequency potential $\phi_{ij}^{-}(x)$. Details about the second order forces are further discussed at Chapter 6.

2.2.3 Floating Rigid Body Motion

Figure 2.2 illustrates a rigid body in waves. The global motions are broken down into six different degrees of freedom: Surge, Sway, Heave, Roll, Pith, Yaw.

The motion of the designed semi-submersible, considering the mooring, is governed by D'Alembert's principle. Particularly, the external forces consist of several components: an added mass component that opposes the body acceleration, a linear damping component proportional to the body velocity, a linear stiffness due to hydrostatic restoring forces, a linear stiffness due to the mooring system and external wave loads. Therefore, the equation, after transformation, can be expressed as,

$$(\mathbf{M}+\mathbf{A}(\omega))\ddot{\eta} + \mathbf{B}(\omega)\dot{\eta} + (\mathbf{C}+\mathbf{K})\eta = \mathbf{F}_w \tag{2.15}$$

where **M** is a 6×6 matrix representing the dry mass and inertia of the structure. **A** represents the added mass coefficients, **B** represents the damping coefficients, **C** represents the hydrostatic stiffness and **K** represents the mooring stiffness. $\mathbf{F}_w$ is a 6×1 vector that contains the wave

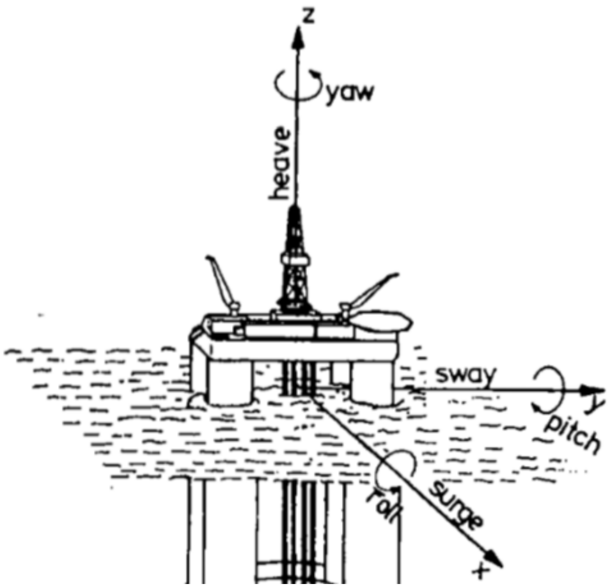

Figure 2.2: Definition of rigid-body motion modes
[31]

excitation force at each degree of freedom.

Corresponding to the first order velocity potential and the second order velocity potential, wave excitation loads and perhaps viscous damping components can also be expressed to the first order accuracy or the second order accuracy. More details are discussed later.

To analyze the motion of a floating wind turbine, some modification is needed to include the wind loads. This is usually done in the time domain because the wind frequencies are hard to relate to the wave frequencies.

2.3 Turbine Aerodynamics

In the mainstream wind turbine simulation tools, such as Aerodyn, the blade element momentum (BEM) theory is used to return the aerodynamic loads on the tower, nacelle and rotor. Force distribution on the blades and hub are also considered.

Due to the presence of two turbines, however, BEM method is not sufficient to take into account both turbines because of the limit of the current code. Instead, the aerodynamic loads could be simplified as two integrated forces onto the rotor center at each time step, as a function of the relative wind velocity under the turbine fixed local coordinate. This can be achieved by an semi-empirical aerodynamic solver TDHMILL, used by Statoil [38].

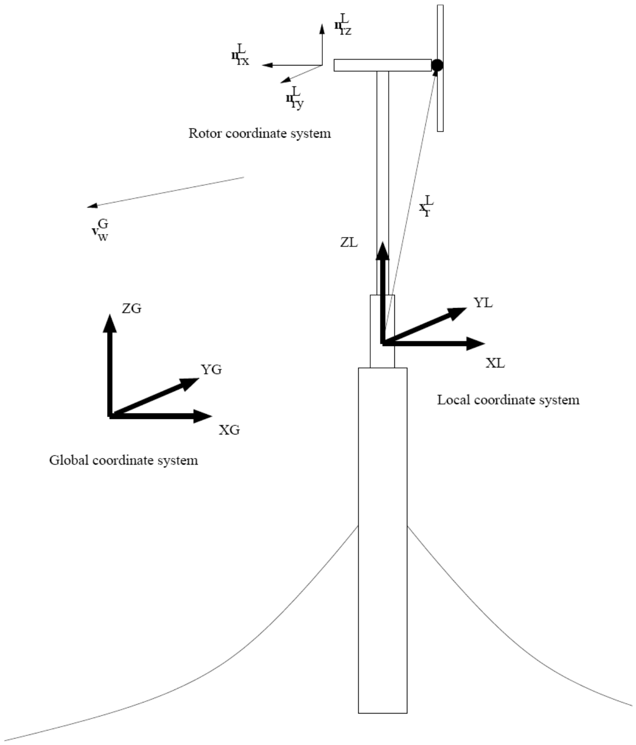

Figure 2.3: Coordinate system and definition
[38]

As demonstrated at Fig 2.3, three coordinate systems are present in the TDHMILL tower model, which are the local hub coordinate, local tower coordinate and the global floater fixed coordinate. In this way, the aerodynamic drag and lift forces are calculated by considering the instantaneous position of elements and the relative wind velocity.

A moment about the local SIMO body coordinate system is also generated. These moments at roll, pitch and yaw are computed in SIMO-Riflex code. Both the forces and moments are transformed into the global coordinate system.

The thrust force is calculated by,

$$T_H(t) = \frac{1}{2}\pi\rho_a R^2 C_T(U_{REL}) U_{REL}^2(t) \tag{2.16}$$

where $U_{REL}(t)$ is the relative velocity between the wind and the rotor hub at time t, C_T is a thrust coefficient given as a function of $U_{REL}(t)$, ρ_a is the mass density of air, R is the rotor radius.

2.4 Wind and Wave Coupled Dynamic Response

Reza etc. reported a hybrid frequency-time domain methods for dynamic responses analysis[32]. This method is also adopted in SIMO [29], the time-domain simulation tool used in this study.

Following the knowledge of rigid body motions in frequency domain, a more sophisticated governing equation considering all the force components might be established in time domain as,

$$(\mathbf{M}+\mathbf{A}(\omega))\ddot{\eta}(t)+\mathbf{B}(\omega)\dot{\eta}(t)+(\mathbf{C}+\mathbf{K})\eta(t)=\mathbf{F}_{WI}+\mathbf{F}_w^{(1)}+\mathbf{F}_w^{(2)}+\mathbf{F}_{cu}+\mathbf{F}_{other}-\mathbf{D_1}\dot{\eta}(t)-\mathbf{D_2}\dot{\eta}(t)|\dot{\eta}(t)| \tag{2.17}$$

where $\mathbf{F}_{WI}$ represents wind force, $\mathbf{F}_w^{(1)}$ and $\mathbf{F}_w^{(2)}$ represent the first order and second order wave force, $\mathbf{F}_{cu}$ is the current drag force. $\mathbf{F}_{other}$ means any other forces, which might include wave drift damping or any other specified forces. $\mathbf{D_1}\dot{\eta}$ is the linear damping force and $\dot{\eta}(t)|\dot{\eta}(t)|$ is the quadratic damping force.

Provided the right hand forces vary sinusoidally at a single frequency ω, equation (2.17) can be rearranged with regards to frequency-dependent components,

$$\mathbf{A}(\omega)\ddot{\eta}(t)+\mathbf{B}(\omega)\dot{\eta}(t)=\mathbf{f}(t)=\mathbf{f}'(t)-(\mathbf{C}+\mathbf{K})\eta(t)-\mathbf{M}\ddot{\eta}(t) \tag{2.18}$$

where $\mathbf{f}'(t)=\mathbf{F}_{WI}+\mathbf{F}_w^{(1)}+\mathbf{F}_w^{(2)}+\mathbf{F}_{cu}+\mathbf{F}_{other}-\mathbf{D_1}\eta(\dot{t})-\mathbf{D_2}\dot{\eta}(t)|\dot{\eta}(t)|$. It should be noted that all components on the right hand side are time dependent.

Both $\mathbf{A}(\omega)$ and $\mathbf{B}(\omega)$ can be further decomposed as a constant term and a frequency dependent term,

$$\begin{cases}\mathbf{A}(\omega)=\mathbf{A}_\infty+\mathbf{a}(\omega)\\ \mathbf{B}(\omega)=\mathbf{B}_\infty+\mathbf{b}(\omega)=\mathbf{b}(\omega)\end{cases} \tag{2.19}$$

where $\mathbf{B}_\infty=0$ for offshore structures.

Equation (2.18) also has a counterpart if all the motions and external forces are considered frequency dependent. With equation (2.19) combined, it can be obtained that,

$$-\omega^2\mathbf{A}_\infty\eta(\omega)+[i\omega\mathbf{a}(\omega)+\mathbf{b}(\omega)]\,i\omega\eta(\omega)=\mathbf{F}(\omega) \tag{2.20}$$

Using the Inverse Fourier Transform and realizing that values of $\mathbf{h}(t-\tau) = 0$ for $t < 0$ and $\tau > t$, equation (2.20) becomes,

$$\mathbf{A}_{\infty}\ddot{\eta}(t) + \int_0^t \mathbf{h}(t-\tau)\dot{\eta}(\tau)d\tau = \mathbf{f}(t) \tag{2.21}$$

substituting $\mathbf{f}(t)$ from Eq. (2.18), the time domain equation of motion becomes,

$$(\mathbf{M}+\mathbf{A}_{\infty})\ddot{\eta}(t)+\mathbf{D}_1\dot{\eta}(t)+\mathbf{D}_2\dot{\eta}(t)|\dot{\eta}(t)|+(\mathbf{C}+\mathbf{K})\eta(t)+\int_0^t \mathbf{h}(t-\tau)\dot{\eta}(\tau)d\tau = \mathbf{F}_{WI}+\mathbf{F}_w^{(1)}+\mathbf{F}_w^{(2)}+\mathbf{F}_{cu}+\mathbf{F}_{other} \tag{2.22}$$

$\mathbf{h}(\tau)$ is the retardation function that can be computed from the frequency-dependant added-mass and damping matrix,

$$\mathbf{h}(\tau) = \frac{1}{2\pi}\int_{-\infty}^{\infty}[\mathbf{b}(\omega) + i\omega\mathbf{a}(\omega)]e^{i\omega t}d\omega \tag{2.23}$$

Using the fact that $\mathbf{b}(\omega) = \mathbf{b}(-\omega)$ and $\mathbf{a}(\omega) = \mathbf{a}(-\omega)$,

$$\mathbf{h}(\tau) = \frac{1}{\pi}\int_0^{\infty}[\mathbf{b}(\omega)cos(\omega\tau) - \omega\mathbf{a}(\omega)sin\omega\tau]d\omega \tag{2.24}$$

Causality of the radiation effect gives $\mathbf{h}(\tau) = 0$ for $\tau < 0$, which leads to $\int_0^{\infty}\mathbf{b}(\omega)cos\omega\tau d\omega = -\int_0^{\infty}\omega\mathbf{a}(\omega)sin\omega\tau d\omega$. For $\tau > 0$, $\mathbf{h}(\tau)$ is hence expressed mathematically as,

$$\mathbf{h}(\tau) = \frac{2}{\pi}\int_0^{\infty}\mathbf{b}(\omega)cos\omega\tau d\omega = -\frac{2}{\pi}\int_0^{\infty}\omega\mathbf{a}(\omega)sin\omega\tau d\omega \tag{2.25}$$

This indicates that retardation function can be found either by the frequency-dependent added mass or potential damping coefficient.

2.5 Solution Method

As discussed above, many external forces and frequency-dependent coefficients are required to solve the responses. In this study, the parameters to be obtained include mass matrix **M**, frequency dependent added mass matrix $\mathbf{A}(\omega)$, potential damping matrix $\mathbf{B}(\omega)$, hydrostatic stiffness matrix **C**, mooring stiffness matrix **K**, first order wave forces $\mathbf{F}_w^{(1)}$, second order wave forces

$\mathbf{F}_w^{(2)}$, wind forces $\mathbf{F}_{WI}$, first order damping matrix $\mathbf{D}_1$ and second order damping matrix $\mathbf{D}_2$.

$\mathbf{M}$, $\mathbf{A}(\omega)$ and $\mathbf{B}(\omega)$ and $\mathbf{C}$ are calculated in GiniE, with a hydrostatic analysis.

$\mathbf{F}_w^{(1)}$, $\mathbf{D}_1$, $\mathbf{F}_w^{(2)}$ and $\mathbf{D}_2$ are computed based on panel model in HydroD by WAMIT method [25]. The frequency domain results are solved in HydroD and results are imported into SIMO, which is a time domain solver, in terms of first order transfer function and second order mean drift forces.

$\mathbf{K}$ is calculated in RIFLEX, where the mooring lines are simulated as bar elements.

$\mathbf{F}_{WI}$ is simplified as concentrated forces applied onto the hubs with the dynamic-link library TDHMILL, which is a simplified wind force tool developed by Statoil.

The current forces $\mathbf{F}_{CU}$ are excluded because the designed site condition is in deep water.

Finally, the time domain equation (2.22) is solved by a coupled SIMO-RIFLEX-TDHMILL method. This is further discussed in Chapter 8

CHAPTER 3

Wind Turbine Properties and Site Condition

Chapter 3 gathers relevant data before the design, essentially the wind turbine data and site condition such as significant wave height, wave period.

3.1 Specification of NREL 5MW Wind Turbine

In the design, NREL 5MW wind turbine is chosen as the designed turbines. NREL 5MW turbine is wildly used in research and is one of the most well documented wind turbines available. The turbine specification information is from NREL report [21].

For low wind speeds($U \leq 3m/s$), the turbine idles until the cut-in speed is reached. Between the range of cut-in and cut-out speed is the operational condition. For higher wind speeds, the blades are feathered and the turbine is either parked or allowed to idle. The Thrust and power output curve as a function of wind speed for NREL 5MW turbine is shown in figure 3.1.

3.1.1 Property

Tower

Table 3.1: General Information about NREL 5MW turbine

Item	Description
Rating	5 MW
Configuration	Upwind, 3blades
Control	Collective pitch
Drive train	Multiple stage gearbox
Rated wind speed	11.4 m/s
Cut-in, Cut-out wind speed	3 m/s , 25 m/s
Cut-in, Rated rotor speed	6.9 rpm, 12.1 rpm
Rated tip speed	80 m/s
Maximum Thrust	~750 kN
Overall Mass	697460 kg
Coordinate Location of Overall CM	(-0.2m,0.0,64.0m)

The tubular tower is made of steel S355, as defined in the European standard DIN EN 10025-2 [1]. Cooresponding material properties are given below.

Table 3.2: General Information of the NREL 5MW Wind Turbine Tower

Young's modulus	210	Gpa
Shear modulus	10	Gpa
Effective density	8500	kg/m^3
Poisson's ratio	0.3	$-$
Height above tower base	87.6	m
Integrated Mass	347,460	kg
CM location to the tower base	38.234	m

The radius and thickness of the tower were designed to be linearly tapered from the tower base to the top. The base diameter is 6 m with thickness of 0.027 m, the top diameter is 3.87 m with a thickness of 0.019 m. Details of the blade is shown in Table 3.3. The distributed tower information is used for building FEM model. "Elevation" is defined as the vertical locations along the tower center-line relative to the tower base. "HtFract" is the fractional height along the tower center-line from the tower base (0.0) to the tower top (1.0).

Hub and Nacelle

The details of mass and location of hub and nacelle are gathered in Table3.4.

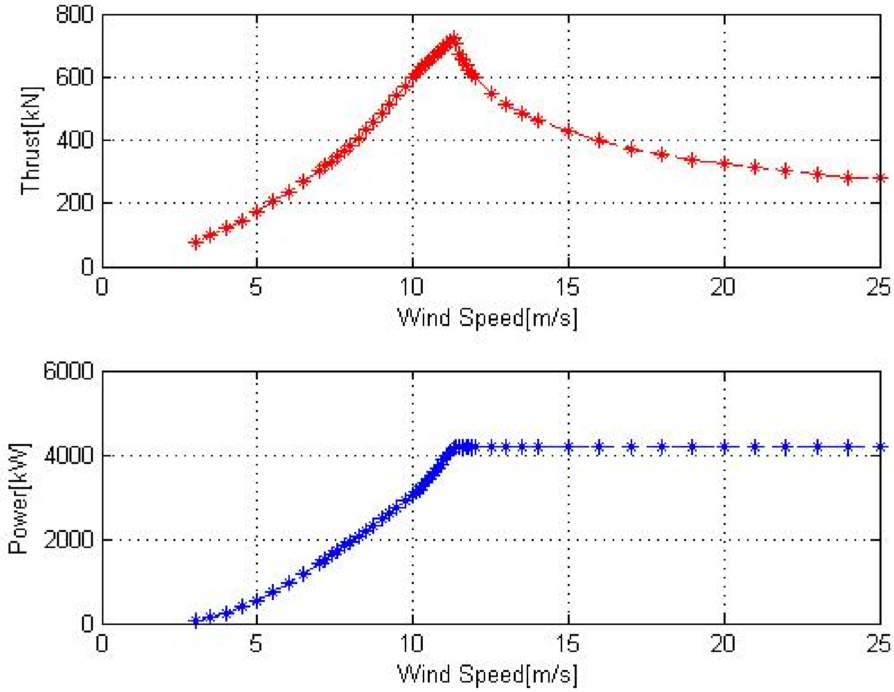

Figure 3.1: Power and Thrust Curve of NREL 5WM Wind Turbine by BEM Method

Blade structure

The length of a blade is 61.5m and the weight of a blade is 17,740kg. Radius are the span-wise locations along the blade-pitch axis with respect to the hub center. BlFract is the fractional distance along the blade-pitch axis from the root(0.0) to the tip(1.0).

3.2 Site Condition

The turbine design is verified under certain cite conditions. Cite condition is crucial to the turbine responses because environmental conditions differs with cite conditions. Important factors to consider when selecting a site are:

1. Site geographic conditions, including location, water depth and distance to shore etc.
2. Average wind and wave energy, described by significant wave height H_s, wave spectral peak period T_p, the mean wind speed $\bar{U}$ and turbulence intensity I.

Table 3.3: Distributed Tower Property

Elevation(m)	**HtFract**$(-)$	**Diameter** (m)	**Thickness**(m)
0.00	0.0	6.000	0.0270
8.76	0.1	5.787	0.0262
17.52	0.2	5.574	0.0254
26.28	0.3	5.361	0.0246
35.04	0.4	5.148	0.0238
43.80	0.5	4.935	0.0230
52.56	0.6	4.722	0.0222
61.32	0.7	4.509	0.0214
70.08	0.8	4.296	0.0206
78.84	0.9	4.083	0.0198
87.60	1.0	3.870	0.0190

Table 3.4: Specifications of Nacelle and Hub

Elevation of Yaw Bearing above Ground	87.6 m
Vertical Distance along Yaw Axis from Yaw Bearing to Shaft	1.96256 m
Distance along Shaft from Hub Center to Yaw Axis	5.01910 m
Distance along Shaft from Hub Center to Main Bearing	1.912 m
Hub Mass	56,780 kg
Nacelle CM Location Downwind of Yaw Axis	1.9 m
Nacelle CM Location above Yaw Bearing	1.75 m
Nacelle Mass	240,000 kg

3. Extreme situation of wind and wave conditions, also described in terms of H_s, T_p, $\bar{U}$ and I.

In this study, the site condition is chosen to be the north sea to the southwest of Norway, whose geographic condition is listed in table 3.6. Lin [27] has thoroughly studied the joint environmental data at this spot. The marginal distributions of $\bar{U}$, the joint distribution of H_s and T_p, the joint distribution of $\bar{U}$,H_s,T_p are given as fitting curves to the measured site condition data.

Following Lin, the most probable value of H_s and T_p are calculated according to chosen value of $\bar{U}$ at hub height. The turbulence intensity is calculated from the IEC standard [20] as a function of mean wind speed. Finally, four condition cases are chosen to be studied, including a under rated condition, the rated condition, an above rated condition and an 50-year extreme condition.

Table 3.5: Distributed Blade Property

Radius(m)	**BlFract**($-$)	**Mass Density** (kg/m)
1.5	0.0	678.935
7.5	0.1	424.054
13.5	0.2	406.186
19.5	0.3	339.333
25.5	0.4	313.820
31.5	0.5	263.343
37.5	0.6	220.638
43.5	0.7	165.094
49.5	0.8	129.555
55.5	0.9	90.248
61.5	1.0	47.028

Location	Water Depth(m)	Distance to Shore(km)
North Sea	202	30

Table 3.6: Site Geographic Condition

Table 3.7: Load cases for operational and extreme condition

Condition	$\bar{U}$ at 90m(m/s)	$H_s(m)$	T_p(s)	$I(-)$	Turbine status
Under rated	8	2	10.3	0.17	Operating
Rated	11.4	2.5	10.2	0.15	Operating
Above rated	16	4.1	10.5	0.13	Operating
Extreme	40	15.6	14.5	0.11	Parked

CHAPTER 4

Initial Design

This chapter elaborates the design procedure of the platform. Since the design of wind turbine platform is not as well-documented as ships or other ocean structures, most of the calculations in the thesis is performed with reference to semi-submersible oil platforms.

4.1 General Requirements

In order to obtain a valid design that could be used for the time domain analysis later. Requirements from different perspectives should be fulfilled.

4.1.1 Configuration

The semi-submersible floater is to be designed to support two NREL 5MW wind turbines. The structure will be made of steel with a proper distribution of water ballast.

The triangular arrangement is adopted in this design because the hydrodynamic feature of a triangular unit will probably be more interesting than a large flat plate and the structure design could possibly be less redundant.

Because of the presence of two turbines, the space between turbines must be adequate and shall not cause significant aerodynamic interaction and blade shedding between two turbines.

4.1.2 Buoyancy

One of the fundamental requirements is that the floater could provide enough water displacement so that the balance between gravity and buoyancy is reached at the designed draft. Specifically, the platform should be equipped with an active ballast system to maintain good floating state while operating.

4.1.3 Stability

The intact stability of floating turbines, according to the DNV rule[35], is evaluated similarly to ship-shaped structures. The general idea is that the floating structure shall be able to

- maintain stability during operation of the wind turbine at the wind speed that produces the largest rotor thrust.
- maintain stability during standstill of the wind turbine in severe storm conditions, which shall be defined in consistence with the metocean conditions of the target environmental class.

The governing equation of hydrostatics is a momentum equilibrium between the rightening moment and the heeling moment. Simply expressed as,

$$M_{heeling} = M_{rightening} \tag{4.1}$$

where

$M_{heeling}$ is caused mainly by the wind load.

$M_{rightening} = \Delta l$, where Δ denotes the total water displacement and l is the horizontal level arm, specifically the distance between center of gravity and center of buoyancy.

The stability requirements for general semi-submersible platforms are, as illustrated in figure 4.1,

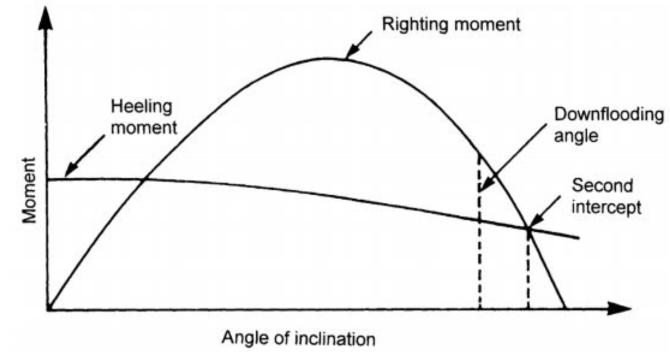

Figure 4.1: Righting Moment and Wind Heeling Moment Curves

- The area under the righting moment curve to the second intercept or down-flooding angle, whichever is less, shall be equal to or greater than 140% of the area under the wind heeling moment curve to the same limiting angle.
- The righting moment curve shall be positive over the entire range of angles from upright to the second intercept.

4.1.4 Motion Characteristics

Natural frequencies are important characteristics in the design because an improper natural frequencies will cause resonance.

Depending on the location and sea state, waves energy typically concentrates at the range of 5 to 20s. In the design phase, attention should be paid to the heave direction such that the natural period at heave does not fall in the range of major wave periods.

4.1.5 Design Procedure

The overall design procedures are summarized as below to ensure a valid initial design.

1. Determine structure components, configuration and dimension
2. Determine the material property and plate thickness
3. Estimation of weight, buoyancy, static heeling angle and heave natural frequencies by empirical formulas

4. Build the FEM model in DNV software GeniE, the floating condition and stability curve are calculated

4.2 Dimension Design

4.2.1 Shedding and Wake Interaction

One problem of great importance for multiple unit wind turbines is that aerodynamic interaction will introduce complicated non-linear effect for the motion. Therefore measures should be taken in the design phase to avoid the aerodynamic interaction between turbines as much as possible. A discussion on the distance between wind turbines is performed to determine a reasonable dimension where the interaction can be neglected. Bjarne [23] thoroughly discussed and formulated the accepted spacing between two turbines.

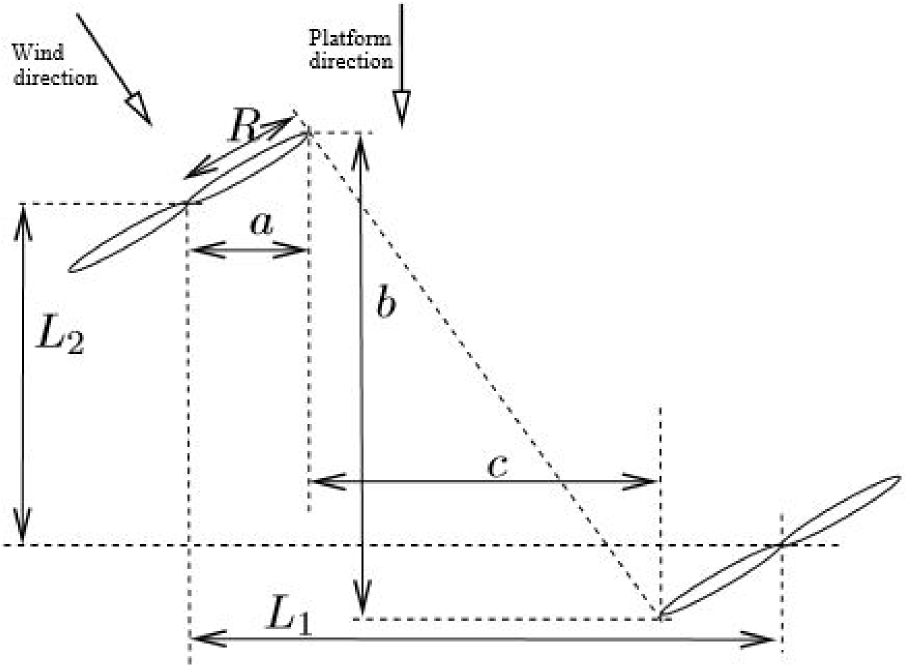

Figure 4.2: Sketch of two turbines in skewed inflow
[23]

Figure 4.2 shows the front and the rear turbines in a triangular configuration. The assumption is valid that the boundary of the wake is unexpanded and steady. The wind direction has an relative oset angle ψ to head-on direction. It also demonstrates the moment when the wake of the front turbine just pass the rear turbine. Horizontal minimum spacing between the two turbines is L_1 for a given inow angle ψ and vertical distance between front turbine and rear turbine is L_2.

From the geometry, the projected distance of the rotor onto the front row plane is given by

$$a = Rcos(\psi) \tag{4.2}$$

The longitudinal distance between front turbine rotor to rear turbine rotor is given by

$$b = L_2 + 2Rsin(\psi) \tag{4.3}$$

Finally the lateral distance between the two rotors is given by

$$c = btan(\psi) \tag{4.4}$$

Introducing the relative measures x and y as $L_1 = xR$ and $L_2 = yR$, the minimum relative distance x for a given inflow angle and longitudinal spacing can be expressed as

$$x = \frac{2 + ysin(\psi)}{cos(\psi)} \tag{4.5}$$

The distance between two turbines, as a calibration of the size of the platform, can be expressed as

$$D = \sqrt{L_1^2 + L_2^2} = R\sqrt{x^2 + y^2} \tag{4.6}$$

In reality, the wake after the turbine will definitely expand. Figure 4.3 sketches an expanding wake:

Normally an expanding wake is shown in figure 4.3 and can be characterized by an expanding angle θ.

$$\theta = arctan(\frac{\sigma_v}{\bar{U}}) \tag{4.7}$$

where

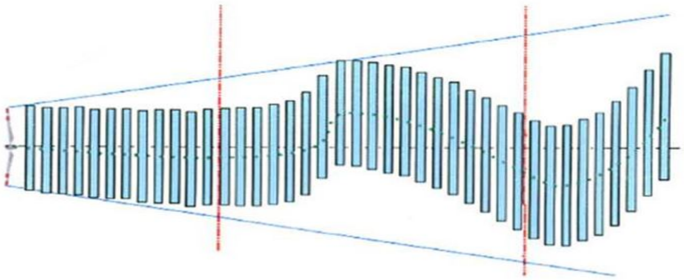

Figure 4.3: sketch of an expanding wake

$\sigma_v = 0.7\sigma_u$. σ_u is the longitudinal turbulence component. $\bar{U}$ is the mean wind speed. For a low turbulence site, as an offshore site, the IEC standard [20] requires that a turbulence intensity $t_i = 0.2$ corresponds to $\bar{U} = 5m/s$ and $t_i = 0.1$ corresponds to $\bar{U} = 25m/s$.

Assigning values to y and ϕ, the relative space x can be calculated from equation (4.5) and plotted in figure 4.4a,

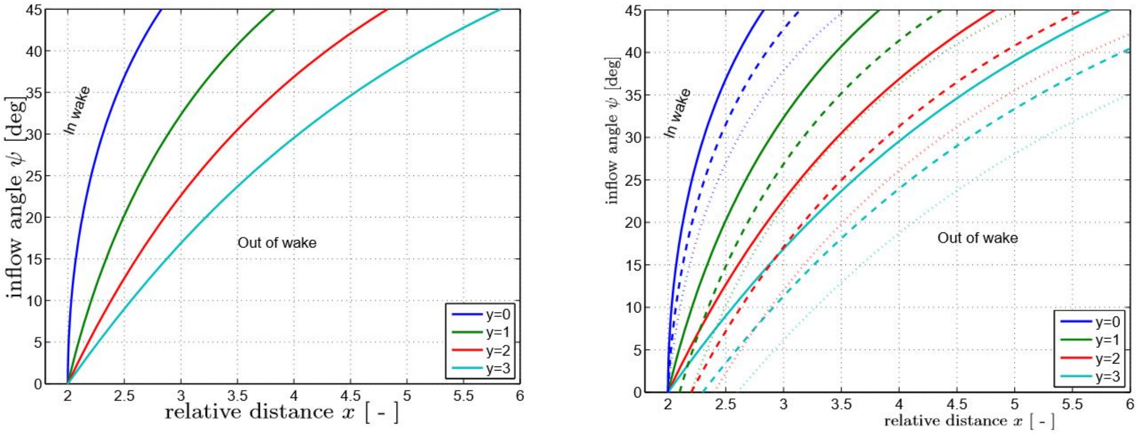

(a) non-expanding wake

(b) expanding wake

Figure 4.4: Relative Distance vs Inflow Angle

Seen from figure 4.4a, the distance between turbines, shown by equation 4.6 reaches minimal given two turbines are aligned in a row. An increasing inflow angle psi demands a greater distance between turbines, due to the shedding effect. This is the condition for steady wake.

To consider the expanding wake, equation (4.7) is combined with equation (4.5). Figure 4.4b shows the results. The solid line denotes unexpanding steady wake. The dashed line denotes $t_i = 0.1$ and dotted line denotes $t_i = 0.2$.

Expanding wake also shows very similar trends in increasing y value and inflow angle ψ

as in unexpanding situation. Additionally, an increasing turbulent intensity factor has to be compensated by further distance.

To minimize the space between the blades and to obtain an arrangement as compact as possible, two turbines should be aligned in a row. The relative distance $y = 0$. The turbine head-on direction may not necessarily in line with the wind inflow direction. A maximum relative angle $\psi_{max} = 15^\circ$ is assumed here.

Turbulent intensity factor in the site conditions varies between $0.13-0.2$. Therefore, it might be reasonable to determine in this design that

$$ti = 0.2$$

Given all the information above, it can be read from 4.4b that the minimum relative distance for insignificant wake interaction and shedding is approximately $x = 2.2$. It is also known that the diameter for the blade of NREL-5MW wind turbine is $R = 61.5[m]$.

From equation (4.6), the distance from turbine rotors becomes,

$$D = L_2 = xR = 2.2 \times 61.5 = 135[m]$$

4.2.2 Draft

A big advantage of semi-submersible platforms, comparing to other floaters such as TLP, is the adjustable draft that allows it to operate in different water depth. Besides, without tension legs or other auxiliary equipments, semi-submersibles are more stabilized by the balance between buoyancy and weight.

For this reason, the draft, which determines the displacement volume, is a very key parameter to maintaining a proper floating condition. As for the initial design, the draft is set to be 20m.

4.2.3 Side Columns

Two side columns are supporting two turbines and the front column will work as a ballast tank trying to balance the uneven weight distribution by the two turbines at the aft. Mooring system will also be connected to the front column too.

The diameter of the side columns(water area inertia) and the distance between side columns(arm of force) are crucial to provide the overturning moment from the wind loads.

Referring to the Windfloat concept, the side column diameter is design to be 10m.

4.2.4 Middle columns

Middle columns are necessary because of a lack of stiffness in such a big offshore structure, given the distance between rotor centers is as long as 135m. Additionally, middle columns also provides buoyancy for vertical equilibrium. The diameter of middle columns are designed to be 6m.

4.2.5 Braces

Braces are adopted for connecting each columns. They should be strong enough to withstand the external loads. Braces also contribute to the water displacement. In this design, a brace diameter of 1.6m is chosen.

4.2.6 Heave plates

The heave plate is added to the structure in order to decrease the motion at vertical degrees of freedom. Therefore the plate has to be thick enough to withstand the hydrodynamic loads.

4.2.7 Conclusion

Main dimensions of the platform is listed in Tab. 4.1. Together with the turbine, the 3D CAD model of the whole structure is demonstrated at Fig. 4.5.

4.3 Weight Calculation

According to the design above, an estimation on structure weight is carried out in Matlab, the data is compared with the results from GeniE, in Tab. 4.2

Table 4.1: Main Dimension for the floater

Draft	20m
Free board	10m
Center column diameter	3m
Side column diameter	5m
Brace diameter	1.6m
Column side to center distance	67.5m
Heave plate edge length	20m
Heave plate height	0.3m
Body plate thickness	0.04m
Heave plate thickness	0.05m
Brace thickness	0.04m

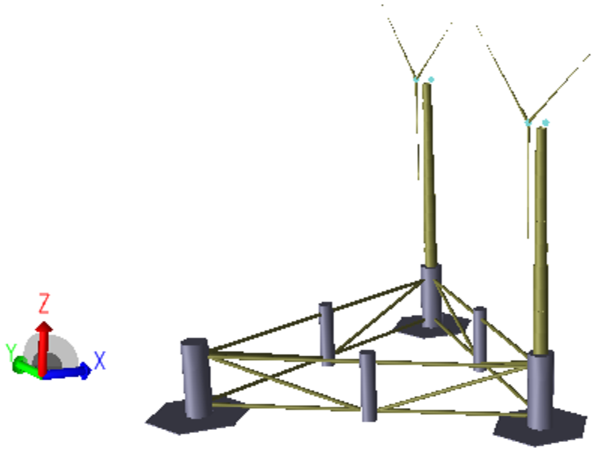

Figure 4.5: Turbine Model and Coordinate System

The hub and nacelle area is small and therefore they are simplified to concentrated point mass during the modelling.

It is seen that the errors from Matlab and GeniE are fairly small. In this way, it can be concluded that the model built in GeniE is valid.

4.4 Buoyancy Calculation

The buoyancy is calculated based on the draft $T = 20m$, the data is gathered in Table 4.5.

Following the GeniE result, the total displacement mass becomes,

$$m_{displacement} = V_{overall} \times \rho_{seawater} = 8563.74 \times 1.025 = 8777.83[t] \tag{4.8}$$

Table 4.2: Mass of the structure without ballast

	Component	**Matlab** $[t]$	**GeniE**$[t]$	**Error** [%]
	Hub	56.78	56.78	0
	Nacelle	240.00	240.00	0
	3 Blades	53.22	53.11	0.206
	Tower	347.46	347.46	0
2 Turbines	Overall	1394.92	1394.71	0.015
	Side Columns	320.60	319.55	0.327
	Middle Columns	183.48	181.29	1.194
	Braces	90.36	90.40	0.044
	Heave plates	799.00	798.90	0.013
Floater	Overall	5587.88	5556.19	0.567
Total		6982.80	6950.90	0.457

Table 4.3: Buoyancy calculation of the semi-submersible platform

Component	**Matlab** $[m^3]$	**GeniE** $[m^3]$	**Error**[%]
Side Columns	1570.8		
Middle Columns	565.49		
Braces	110		
Heave plates	311.77		
Overall	8667.80	8563.74	1.2

4.5 Ballast Design

Having had the results from weight and buoyancy calculation, the volume required for ballast can be calculated as:

$$V_{ballast} = \frac{m_{displacement} - m_{weight}}{\rho_{seawater}} = 1782.37[m^3] \tag{4.9}$$

Tab. 4.4 shows the needed ballast volume in comparison with the available ballast volume. It is seen from the Tab. 4.4 that the space can be used for ballast is much more than the ballast space needed. For maximum usage of the long moment arm, the ballast should be distributed on side columns.

The ballast distribution is influenced by not only vertical equilibrium between weight and buoyancy, but also by the overturning moment from turbines, which is correlated to wind speed

Table 4.4: Available spaces for ballast

Space	**Volume** $[m^3]$	**Used as ballast?**
Side Columns	7068.60	Yes
Middle Columns	2544.70	No
Braces	2041.40	No
Heave plates	935.30	No
Overall	12590	1782.37 m^3

Table 4.5: Ballast distribution of different wind speed

Wind speed(m/s)	**Column1** $[t]$	**Column2** $[t]$	**Column3**$[t]$
0	1570.8		
8	565.49		
11.4	110		
25	311.77		
49	8667.80	8563.74	1.2

as shown in Fig. 3.1.

Assuming the center of rotation is at the center of buoyancy, the overturning moment can be estimated by,

$$M_{overturning}^{max} = Thrust_{max} \times (z_{hub} - z_B) = 1500 \times (100 + 11.46) = 167190 kN \cdot m \tag{4.10}$$

4.6 Hydrostatic Analysis

The hydrostatic analysis is carried out in GeniE. Finite Element Model is built and then exported into HydroD for static analysis.

4.6.1 Hydrostatic hand calculation

Assuming the incident wind comes from x-axis, the most dangerous rotation axis in this case would be the pitch motion with respect to y-axis.

When a body is freely floating, the restoring moments are caused by the hydrostatic pressure.

The restoring term may be written as a function of heeling angle,

$$F_k^R = -C_{kj}\eta_j \tag{4.11}$$

where C_{kj} is defined as restoring coefficients.

By analytical solution, neglecting the coupling effect from other degree of freedom, the pitch restoring coefficient C_{55} can be calculated by, [36]

$$C_{55} = \underbrace{\rho g V(z_B - z_G)}_{(1)} + \underbrace{\rho g \iint_{A_{WP}} x^2 \, ds}_{(2)} = \rho g V \overline{GM}_L \tag{4.12}$$

where V is the displaced volume, z_B and z_G are the z coordinates of center of buoyancy and center of gravity. A_{WP} is the water plane area and $\overline{GM}_L$ denotes the longitudinal meta-centric height. Equation (4.12) shows clearly two contributions to the longitudinal metacentric height: part (1) from the distance between center of buoyancy and center of gravity, part (2) from the water area inertia.

According to the output from HydroD,

$$G\bar{M}_L \approx 35m$$

Therefore, inserting values into Equation 4.12,

$$C_{55} = 1025 \times 9.81 \times 8563.74 \times 35 = 3013869[kN \cdot m/rad]$$

Combined with the maximum overturning moment estimated from Equation (4.10), the pitching angle is calculated as,

$$\dot{\eta}_5 = \frac{M_{overturning}}{C_{55}} = 0.0555 rad = 3.18^\circ$$

4.6.2 GeniE Modeling

Panel Model

A panel model is built to describe the geometry of the structure in hydrostatic and dynamic analysis. The water pressure from water is also assigned to the panel model as a property. Wetted surfaces in the panel model are discretized by finite element method. Figure 4.6 shows the panel model of the submerged floater. Parts in green are the discretized panels and the yellow outer-layers are the attributed water pressure.

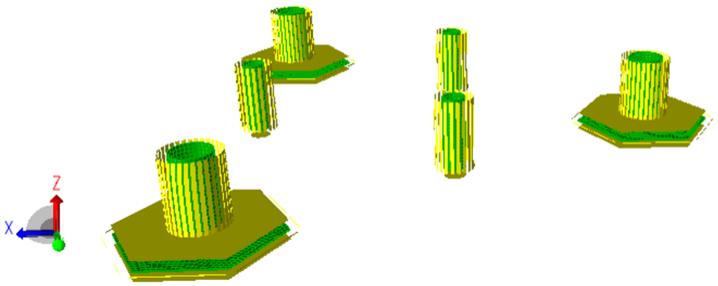

Figure 4.6: Panel model with the static water pressure

Mass Model

A mass model contains all the mass information of the whole structure and is built and discretized into finite elements before hydrostatic and hydrodynamic analysis.

As shown in Figure 4.7, the towers and blades are modeled with beam elements because of varied cross-section area while as the semi-submersible platform is modelled with shell elements. The hub and nacelle mass information is presented as point mass and are connected to other structures by weightless beam elements.

For simplicity, the ballast water inside of side columns are modelled by beam elements with the same density and properties as sea water. The yellow points represent point mass

4.6.3 Stability Behaviour

The result returned from HydroD demonstrates that the equilibrium of pitch is reached at $\dot{\eta}_5 = 3.01°$, which is very close to the hand calculation value 3.18°. Figure 4.8 shows the GZ-curve generated from HydroD,

The heeling moment comes from the maximum thrust of wind turbines, which represents the most dangerous situation. It is reported from HydroD that the GZ-curve zero crossings are

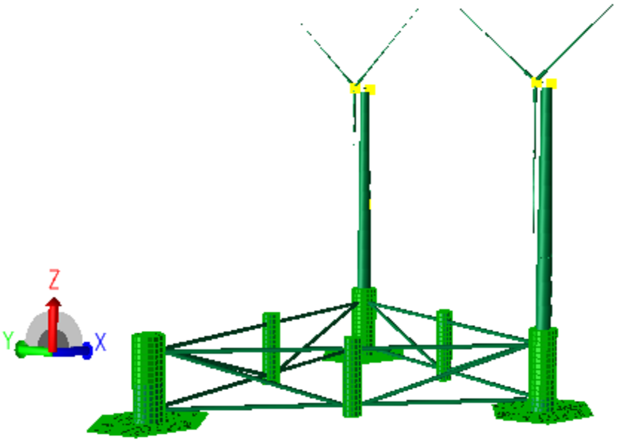

Figure 4.7: Overall Mass Model

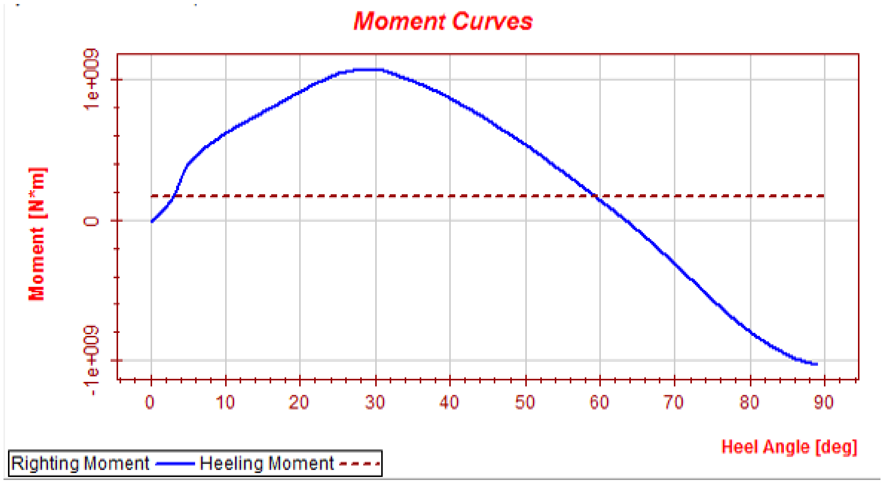

Figure 4.8: Restoring Moment Curve

at 0.23° and 63.33°, indicating that the structure possess a good floating condition with the designed ballast in this case. The rightening moment stays positive from upright to the second intercept.

Because the side column is water tight, the downooding angle is chosen to be identical to the second intercepting angle. The requirements for intact stability is fulfilled since the area under the righting moment to the second intercept angle is apparently greater than 140% of the area under the wind heeling moment curve to the second intercept angle.

To recapitulate, the design satisfy the intact stability requirements from DNV.

CHAPTER 5

First Order Frequency Domain Analysis

5.1 Force Models

The first order frequency domain analysis is performed assuming a linear system. For this semi-submersible, the first order motion is governed by,

In the first order frequency analysis, mooring system is not included and only the first order natural frequency is considered. Specifically for this semi-submersible turbine, the governing equation of linear hydrodynamics can be presented as,

$$(\mathbf{M}+\mathbf{A}(\omega))\ddot{\eta}+(\mathbf{B}(\omega)+\mathbf{D_1})\dot{\eta}+\mathbf{C}\eta=\mathbf{F}_w^{(1)} \tag{5.1}$$

where $\mathbf{M}$ is the structural mass/inertia matrix, $\mathbf{A}(\omega)$ is the frequency dependent added mass matrix, $\mathbf{B}(\omega)$ is the linear potential damping matrix, $\mathbf{D_1}$ is the linear viscous damping matrix and $\mathbf{C}$ is the hydrostatic stiffness matrix. Notably, the external force here is the first order wave force.

5.1.1 Morison Equation

Morison equation is a semi-empirical equation used to estimate the wave loads for slender structures when the structure diameter D is small compared to the wavelength λ, roughly, $D/\lambda < 5$ [31].

From Morison's formula, transverse force per unit length on structures in waves is expressed as,

$$dF = \underbrace{\rho\pi\frac{D^2}{4}\dot{u}}_{\text{Froude-Krylov Force}} + \underbrace{\rho C_a\pi\frac{D^2}{4}(\dot{u}-\dot{v})}_{\text{Added Mass Force}} + \underbrace{\frac{1}{2}\rho C_D D(u-v)|u-v|}_{\text{Drag Force}} \tag{5.2}$$

where C_a is the added mass coefficient. In the study, $C_a = 1.2$ is adopted. C_D is the drag coefficient, u is the transverse wave particle velocity and v is the local transverse local velocity. It is seen that the frequency dependent added mass matrix $\mathbf{A}_\omega$ is related to $\frac{D^2}{4}\pi\rho C_a$

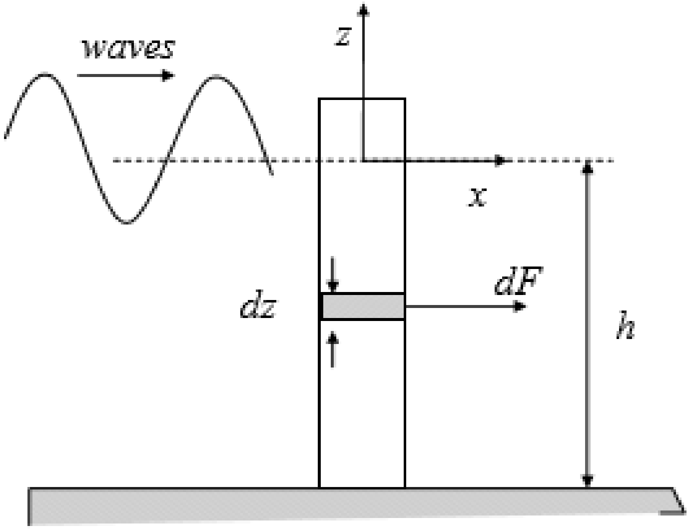

Figure 5.1: Horizontal submerged vertical cylinder
[18]

5.1.2 Linearization of the Drag Force

It is known that the structure responses with first order wave potential theory are often assumed in a sinusoidal form.

According to Morison equation, however, the drag force term $\frac{1}{2}\rho C_D D(u-v)|u-v|$ brings a mathematical difficulty to the solution of the linear system. Some efforts have been made to linearize the drag force so that a sinusoidal ansatz could maintain.

Regular wave is described by sinusoidal function and a regular wave velocity become,

$$u = u_0 sin(\omega t) \tag{5.3}$$

Out of a linear system assumed, the response of the structure will also be harmonic, however, with a phase shift to the incident waves.

$$\eta = \eta_1 cos(\omega t) + \eta_2 sin(\omega t) \tag{5.4}$$

The relative velocity can be calculated as,

$$u_r = u - v = u - \dot{\eta} = Acos(\omega t + \phi) \tag{5.5}$$

where $A = \sqrt{(\omega\eta_1)^2 + (u - \omega\eta_2)^2}$ and ϕ represents a phase shift.

If ϕ in equation (5.5) is neglected, the nonlinear drag force can be written as,

$$dF_{drag} = \frac{1}{2}\rho C_D D A^2 |cos(\omega t)| cos(\omega t) \tag{5.6}$$

where D is the diameter of the column and dF represents the drag force for a vertical length of dz

Introducing a linearized coefficient K_L and assuming the drag force can be expressed as,

$$dF_{drag,L} = \frac{1}{2}\rho C_D D K_L A cos(\omega t) \tag{5.7}$$

The coefficient K_L can be decided by setting the work done by non-linearized and linearized drag force equal over a very long period of time. Mathematically expressed as,

$$\int_0^T (dF_{drag} - dF_{drag,L}) u_r dt = 0 \tag{5.8}$$

From the equation, the expression of K_L is obtained,

$$K_L = \frac{A\int_0^T |cos(\omega t)| cos(\omega t)^2 dt}{\int_0^T cos(\omega t)^2 dt} = \frac{8A}{3\pi} \tag{5.9}$$

Therefore, equation (5.7) is simplified to, as a linear function of $cos(\omega t)$

$$dF_{drag,L} = \frac{4\rho C_D D A^2}{3\pi} cos(\omega t) \tag{5.10}$$

In frequency domain analysis, the linear drag coefficient $\mathbf{D}_1$ is related to $\frac{4\rho C_D D A^2}{3\pi}$.

5.1.3 Transfer Function

From equation (5.2), the first order wave excitation force $\mathbf{F}_w^{(1)}$ consists of Froude-Krylov loads and diffraction loads.

$$dF_w^{(1)} \approx \underbrace{\rho\pi\frac{D^2}{4}\dot{u}}_{\text{Froude-Kriloff loads}} + \underbrace{\rho\pi\frac{D^2}{4}C_a\dot{u}}_{\text{diffraction loads}} \tag{5.11}$$

Because of a deep water site condition, $\omega^2 = gk$, the wave velocity can be expressed as,

$$\dot{u} = \omega^2 \zeta e^{kz} cos(\omega t - kx) \tag{5.12}$$

where ω is the wave angular frequency, ζ is the wave amplitude.

Normally, transfer function is defined to express the wave force, which shows the wave forces in unit wave height. Combining Eq. (5.11) and Eq. (5.12), the transfer function on the submerged slender structure is given by,

$$H_w(\omega) = \frac{f}{\zeta} \approx \rho V(1 + C_a)\omega^2 e^{(\omega^2 z/g)} \tag{5.13}$$

where V is the submerged volume and f is from $\mathbf{F}_w^{(1)} = f e^{i\omega t}$

In a more general form, the force transfer function is also related to wave incident angle β, the excitation loads might be expressed in a matrix form as,

$$\mathbf{F}_w^{(1)} = \zeta \mathbf{H_w}(\omega, \beta) e^{i\omega t} \tag{5.14}$$

where $\mathbf{H}(\omega,\beta)$ is dependent on the specific expression of Found-Kriloff loads and diffraction loads at certain wave direction.

Combining equation (5.1) and equation (5.14) and using the complex ansatz of the motion response $\eta = \eta_a e^{i\omega t}$, the governing equation can be weritten as,

$$[-\omega^2(\mathbf{M}+\mathbf{A}(\omega)) + i\omega(\mathbf{B}(\omega)+\mathbf{D}_1)+\mathbf{C}]\eta_a = \zeta\mathbf{H}_w(\omega,\beta) \tag{5.15}$$

Typically, responses in the frequency domain is defined by a response amplitude operator (RAO), which is the transfer function between a particular response and the wave elevation,

$$\mathbf{RAO}(\omega,\beta) = \eta_a(\omega)/\zeta_a = [-\omega^2(\mathbf{M}+\mathbf{A}(\omega)) + i\omega(\mathbf{B}(\omega)+\mathbf{D}_1)+\mathbf{C}]^{-1}\mathbf{H}_w(\omega,\beta) \tag{5.16}$$

The RAO is a very critical statistic in frequency domain analysis and as clearly shown in the equation above, RAO are usually calculated for all ship motions and for all wave headings.

5.2 Wave Spectrum

In section 3.2, four site conditions are chosen as the designed conditions in the study. Fig. 5.4 demonstrates four JONSWAP wave spectra from these four conditions.

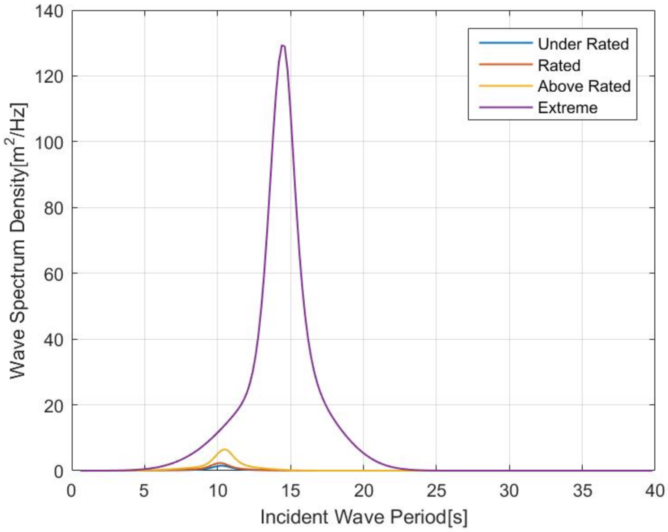

Figure 5.2: The JONSWAP spectra comparison

It is seen clearly that the peak of each spectrum does not overlap; this is because of the different T_p of each condition. On the other hand, H_s determine the spectrum density amplitude; the extreme condition is significantly higher than other conditions. From the spectra, it is safe to say that the hydrodynamic responses under extreme condition would be more vulnerable. Therefore, the hydrodynamic analysis in frequency domain is performed under extreme situation.

It should also be noted that the spectra mainly are distributed within $[5s, 25s]$. This requires the simulation to be run at least within the frequency domain $[0.25Hz, 1.25Hz]$.

5.3 Modelling

5.3.1 Morison Model

Morison model is created on top of mass model and panel model, to calculate the viscous drag forces. GeniE requires that all the components modelled in the Morison model must be beam elements. Some adjustment has therefore been done to the heave plates, to transfer the heave plates from hexagon to circular beam.

According to DNV rules [2], Morison's formula is applicable if

$$\lambda > 5D \tag{5.17}$$

where λ is the wave length and D the diameter of the columns.

The site conditions gives the mean wave period $T_{mean} \geq 10s$. By the dispersion relation for deep water, the mean wave length is calculated,

$$\lambda_{mean} = \frac{gT_{mean}^2}{2\pi} \approx 156[m] \tag{5.18}$$

The ratio between mean wave length and maximum diameter is

$$\frac{\lambda_{mean}}{D_{max}} = \frac{156}{10} = 15.6 \geq 5 \tag{5.19}$$

Therefore, in this case, the long wave approximation is satisfied, and hence Morison equation is applicable. Figure 5.3 demonstrates the Morison model.

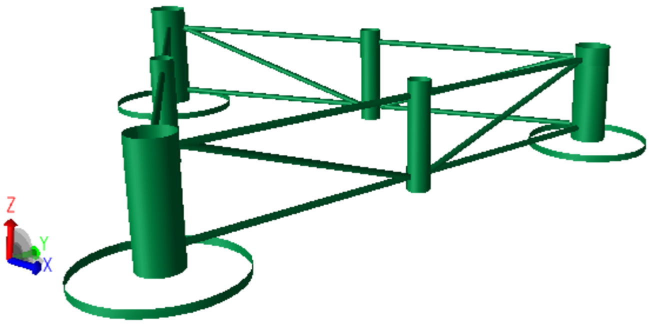

Figure 5.3: Morison Model at GeniE

5.3.2 Drag Coefficient

As shown in Eq (5.10), the parameter C_D is key to determine the viscous damping of each components.

In GeniE, however, the Morison model will be counted as buoyancy if volume property is assigned to it. Therefore, the dimension of the Morison model should be scale down to a negligible extent. The viscous drag, on the other hand, should maintain the same as the original components. Assuming a scale down factor of $K_s = 0.1\%$, the scaled diameter becomes

$$D' = K_s \times D = 0.1\% D \tag{5.20}$$

The additional volume influence from Morison model becomes,

$$V' = \left(\frac{D'}{D}\right)^2 V = (0.1\%)^2 V \tag{5.21}$$

It can been seen that, by a scale down factor of 0.01%, V' is fairly negligible compared to the original volume V. Following the condition in equation (5.20), the drag coefficient should be scaled up accordingly to maintain the viscous effect, the scale up factor is

$$C_D{}' = \frac{C_D D}{D'} = 1000 C_D \tag{5.22}$$

For circular cylinders, drag coefficient C_D is a function of Reynolds number, K_C number and surface roughness. According to DNV rules [2], assuming the steel surface is newly painted and smooth, the surface roughness is

$$\Delta = \frac{k}{D} < 10^{-4}$$

where $k = 5 \times 10^{-5}$ for newly painted surfaces.

The drag coefficient on roughness is then taken as,

$$C_{DS}(\Delta) = 0.65$$

K_C number is big under this extreme sea state condition, for conservation, it is chosen that $K_C = 12$. The wake amplification factor is taken as,

$$\begin{cases} C_\pi = 1.50 - 0.024 \cdot (12/C_{DS} - 10) \\ \Psi(K_C) = C_\pi + 0.10(K_C - 12) \\ C_D = C_{DS}(\Delta) \cdot \Psi(K_C) \end{cases} \tag{5.23}$$

Following the calculation, a reasonable drag coefficient for cylinder is $C_D = 0.843$ and the force is perpendicular to the components. For the rectangular shaped heave plates, the drag coefficient is referred to from the study carried out by S.R.Munshi [34], as in figure 5.4

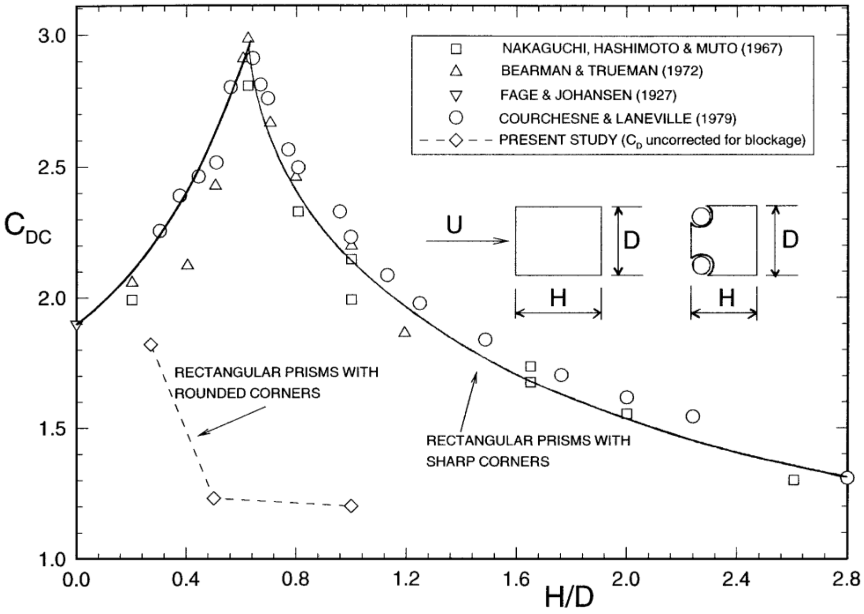

Figure 5.4: Aspect ratio vs Drag coefficient of rectangular plates

The figure clearly shows that when $\frac{H}{D} \rightarrow 1$, $C_D \approx 2.2$ and that when $\frac{H}{D} \rightarrow 0$, $C_D \approx 1.9$. Therefore, for the heave plates, the drag force for vertical motion is chosen as $C_{Dz} = 2.2$, and the drag force for horizontal motion is chosen as $C_{Dy} = 1.9$. For braces, however, because the buoyancy contribution from braces should be counted, there will not be any scale down on the brace components. The drag coefficient are calculated and listed in table 5.1.

Table 5.1: Drag coefficient of each submerged component

Components	$D[m]$	$D'[m]$	$C'_D[-]$
Side columns	10	0.01	843
Middle columns	6	0.006	843
Heave plates	34.6	0.0346	1900
Braces	1.6	1.6	0.843

5.4 Mesh Convergence Study

A crucial issue for FEM analysis is to verify the convergence of the results. To ensure the analysis is done based on solid numerical results, a mesh convergence study is carried out thoroughly.

Simple calculations are done to estimate a qualified mesh size as a reference. GeniE users manual [17] requires that, the element diagonal in the panel model shall not exceed 1/4 of the wave length. Assuming the mesh are all perfectly square,

$$l_{mesh} \leq \frac{1}{4\sqrt{2}}\lambda \tag{5.24}$$

where λ is the incident wave length.

From a dispersion relation, the wave length λ can be expressed as,

$$\lambda = \frac{gT^2}{2\pi} \tag{5.25}$$

Therefore, the largest mesh length is limited by,

$$l_{mesh}^{max} \leq \frac{1}{4\sqrt{2}}\lambda_{min} = \frac{1}{4\sqrt{2}}\frac{gT_{min}^2}{2\pi} \tag{5.26}$$

As shown in the wave JONSWAP spectrum in figure , wave energy is mainly distributed in the wave period range from 5s to 25s; the rage out side of this generally causes little response due to the low spectrum density. To be safe, the smallest wave period is taken as $T_{min} = 3s$.

Inserting into equation (5.26),

$$l_{mesh}^{max} \approx 2.5 \tag{5.27}$$

Practically, a mesh size of 2.5m should possibly return a good results. Five mesh sizes are chosen to check the sensitivity of the resolution to mesh density.

Table 5.2: Mesh Size Comparison

Mesh Level	**Mesh Size** $[m^2]$	**Number of Elements**
Coarse Mesh	4×4	808
Medium Mesh 1	3×3	1570
Medium Mesh 2	2.5×2.5	1960
Medium Mesh 3	2×2	2752
Fine Mesh	1.5×1.5	5388

Implementing in the simulation, 5 meshes with different density are generated. Figure 5.5 visually shows a comparison between mesh density 1.5 × 1.5 and 4 × 4.

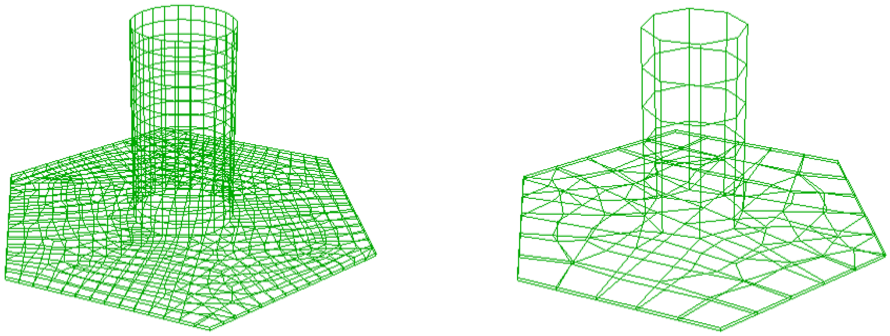

Figure 5.5: Fine Mesh vs Coarse Mesh

To validate the results, heave response amplitude operators under wave direction 0° are calculated and compared in figure 5.6.

It should be noticed that the output of 1.5 × 1.5 and 2 × 2 are completely overlapped, indicating that the mesh size 2 × 2 could be a good balance between the accuracy and computational effort.

2.5 × 2.5 is less accurate around the first peak $f \approx 0.2Hz$, which is the eigenfrequency of the platform in Heave. This is not exactly as what shows in equation (5.27), but $2.5m$ seems to be a mesh quite close to the converged values.

3 × 3 failed to capture the first peak at all; 4 × 4 just gives a quite distorted RAO.

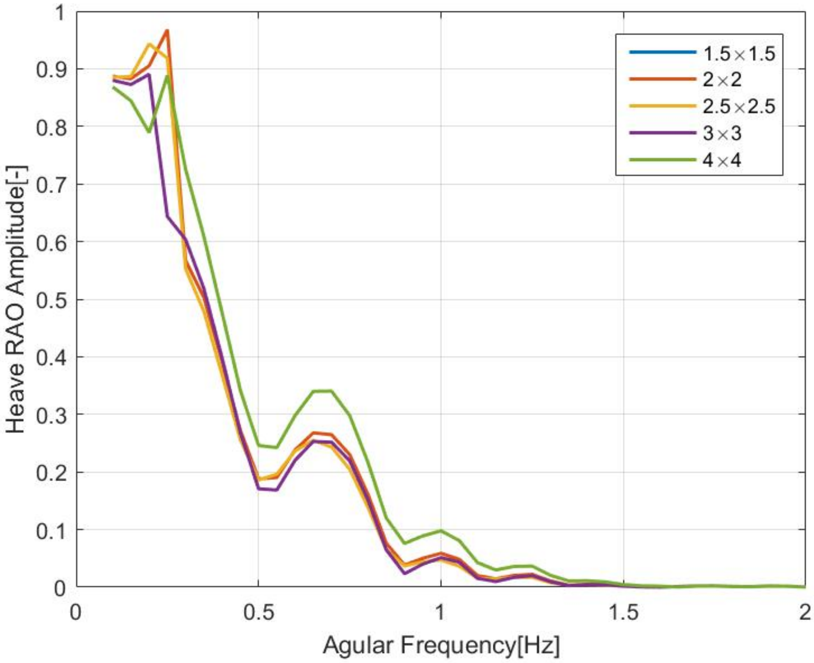

Figure 5.6: Heave RAO under different mesh density

Therefore, it might be reasonable to decide that the mesh size used for the submerged parts are $2m \times 2m$.

5.5 Eigenfrequency Analysis

Eigenfreqeuncy is an important characteristic for any structures exposed to oscillating loads. At its eigenfrequency, a system tends to resonate with the excitations and reaches extraordinary responses. To avoid the resonance of the designed turbine, two types of frequencies should be compared to the eigenfrequencies of the structures:

- The wave spectrum

- Eigenfrequencies of the turbine rotor

5.5.1 Eigenfrequencies of the floating turbine

For an undamped system with no excitation loads, equation of the motion could be simplified to the eigenvalue problem,

$$(-\omega^2(\mathbf{M}+\mathbf{A}(\omega))+(\mathbf{C}+\mathbf{K}))\eta = 0 \tag{5.28}$$

where **K** is the hydrostatic stiffness from mooring system.

The non-trivial condition to satisfy the equation is that,

$$det(-\omega^2(\mathbf{M}+\mathbf{A}(\omega))+(\mathbf{C}+\mathbf{K})) = 0$$

Consider an uncoupled situation at each degrees of freedom, a good approximation for eigenfrequencies of the structure can be written as,

$$\omega_{jj} = \sqrt{\frac{C_{jj}+K_{jj}}{M+A_{jj}}}, j = 1,2,..6 \tag{5.29}$$

From equation (5.29), the eigenfrequency of each DOF is essentially determined by the sum of hydrostatic stiffness coefficient C and mooring stiffness coefficient K and the sum of structure mass and added mass.

Because of the body symmetry with respect to x-z plane, the restoring coefficients are 0 at horizontal DOFs, simply because there is no hydrostatic restoring force,

$$C_{11} = C_{22} = C_{66} = 0 \tag{5.30}$$

The analytical solution of the restoring coefficients at vertical DOFs can be expressed explicitly as [31],

$$\begin{cases} C_{33} = \rho g A_{WP} \\ C_{44} = \rho g V \overline{GM}_T \\ C_{55} = \rho g V \overline{GM}_L \end{cases} \tag{5.31}$$

where A_{WP} is the water plane area, V is the displaced volume of water, $\overline{GM}_T$ and $\overline{GM}_L$ are the transverse and longitudinal metacentric height respectively.

On the other hand, the mooring stiffness is not included yet, which gives,

$$K_{jj} = 0 \tag{5.32}$$

Eigenfrequencies at six DOFs are obtained by combining Eq. (5.29)-Eq. (5.32).

Table 5.3: Eigenfrequcny from Wadam

Eigenvalue	**Surge**	**Sway**	**Heave**	**Pitch**	**Roll**	**Yaw**
Frequency [rad/s]	0	0	0.247	0.201	0.201	0
Period [s]	∞	∞	25.488	31.215	31.210	∞

Table 5.3 shows the eigenfrequency values at each degree of freedom calculated by Wadam. It can be seen that at surge, sway and yaw directions, the eigenfrequencies are 0. Eigenfrequencies at pitch and roll are comparable because this turbine has similar size in x direction and y direction, leading to close hydrostatic stiffness at these two DOFs.

5.5.2 Eigenfrequency Discussion

As shown in figure 5.4, the wave spectrum distributes mainly within the range of $T \in [5s, 25s]$. The eigenperiod for heave, pitch and roll, as listed in table 5.1 are excluded from that range. It might be safe to say that the wave introduced motion will not cause a significant resonance for the designed structure.

Another excitation that might brings resonance is the rotation of the blades. The rotational frequency 1P and the passing frequency of the blades 3P are important characteristics. Both 1P and 3P are determined by the rotational frequency of the rotor. The cut-in and rated rotor speed, listed in table 3.1, are used to calculate the range of 1P and 3P.

Frequency	**Minima**	**Maxima**
Rotational Frequency	6.9rpm	12.1rpm
1P	$1.098Hz$	$1.926Hz$
3P	$3.294Hz$	$5.778Hz$

For the NREL 5MW wind turbine, the calculated frequency range of 1P is $[1.098Hz, 1.926Hz]$ and the frequency of 3P is $[3.294Hz, 5.778Hz]$. As comparison, the structure eigenfrequencies are $0.247Hz$(Heave) and $0.201Hz$(Pitch and Roll). This indicates the turbine is spinning much faster under operating conditions than the eigenvalue situations of hydrodynamic motions. The resonance is therefore not likely to be aroused by turbine spinning.

5.6 RAO Analysis

The motion responses are described by response amplitude operator(**RAO**). From a linear system perspective [12], given RAO and wave spectra, responses can be obtained as below,

$$S_{\eta}(\omega) = \mathbf{RAO}^2 \cdot S_{\xi}(\omega) \tag{5.33}$$

where S_{η} is the frequency domain response spectrum. **RAO** is the response amplitude operator and S_{ξ} is the wave spectrum in frequency domain.

Specifically, horizontal degrees of freedom are important from a hydrodynamic point of view. However, the most critical degrees of freedom are pitch due to the wind loads. Surge, Sway and Yaw RAOs are not discussed in this chapter because the mooring system is not included yet and therefore the RAOs of these directions approaches at $\omega = 0$ and decline as ω increases.

Calculations are done for different wave incident angle, considering head sea, bow sea, beam sea, quartering sea and following sea situations. The wave incident angle only covers $[0°, 180°]$ because of the x-z symmetry.

5.6.1 Heave RAO

Figure 5.7a shows the RAOs in heave. It can be seen that peaks are at around $0.25[Hz]$ from all the 5 directions, which is the eigenfrequency of the structure at heave direction. But the resonance is quite limited at the eigenfrequency. This is because the heave damping for this structure is fairly large, considering gravity, added mass and the effect from heave plates.

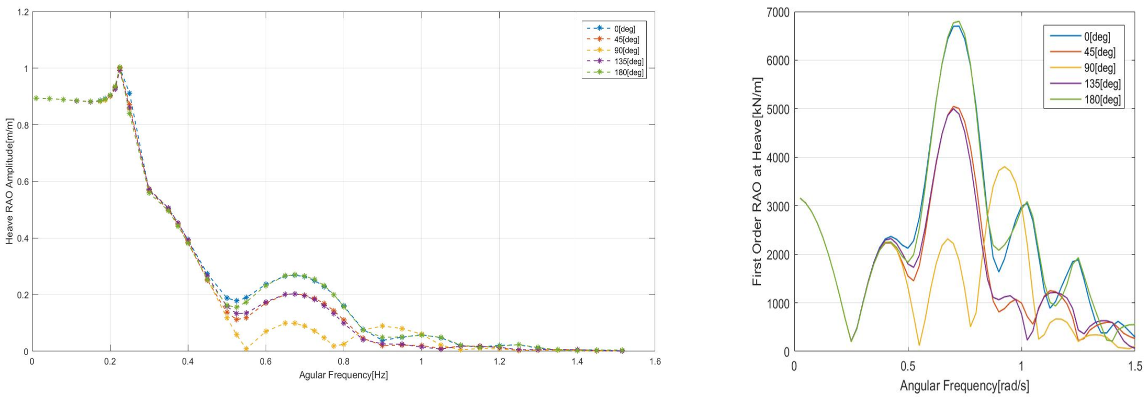

(a) Motion

(b) Force

Figure 5.7: Heave RAO

Generally, peaks in figure 5.7a correspond very well with the peaks of force amplitude RAO in figure 5.7b. A clear causal relationship is confirmed between the external forces and responses, with the exception of eigenfrequencies, where the resonance is excited and large responses are expected.

It should also be noted that heave motion is a translation degree of freedom, which makes Heave RAO generally takes different shapes of pitch RAO and roll Rao. Figure 5.7a can be physically interpreted as: when free floating in the water, the heave amplitude of the wind turbine will be quite close to the wave amplitude within $\omega \in [0Hz, 0.25Hz]$ because the corresponding heave RAO is close to 1. When the wave frequency gets higher, the wave length becomes less significant, so does the heave motion.

5.6.2 Pitch RAO and Roll RAO

Pitch RAO is demonstrated in figure 5.8b. It can be seen that the results of 0° and 180°, 45° and 135° are overlapping quite well. The amplitude of pitch RAO at 0° and 180° are also higher than that of 45° and 135° because part of the wave energy are causing Roll motion at bow sea and quartering sea, which can be seen in figure 5.9b.

Similar situations are observed in roll direction. The major difference is that the Roll RAO amplitude becomes negligible at 0° and 180° while as Pitch RAO is non-zero at 90°. These phenomena confirm the x-z symmetry of the structure.

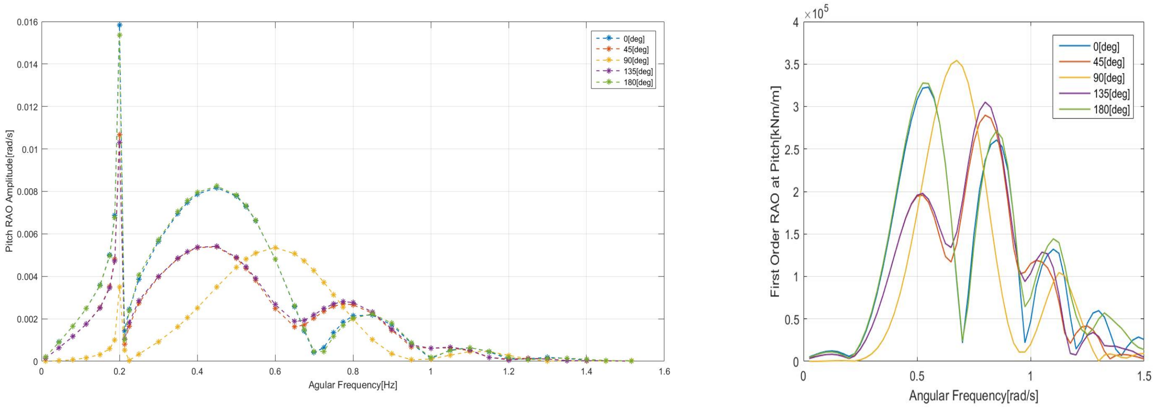

(a) Motion

(b) Force

Figure 5.8: Pitch RAO

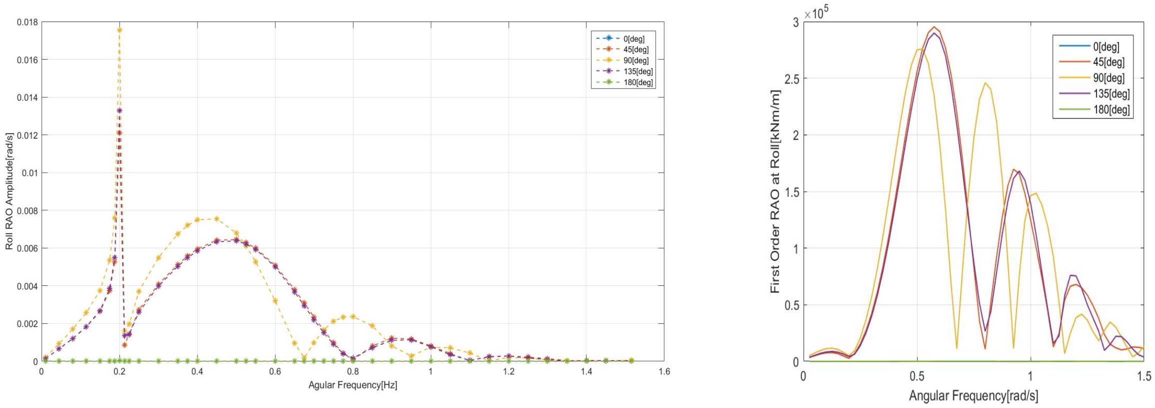

(a) Motion

(b) Force

Figure 5.9: Roll RAO

From both figures, peaks are observed around $0.2Hz$, which is the eigenfrequency of the structure. The second peaks corresponds to the highest wave spectrum density wave frequency as shown by the extreme condition spectrum in figure 5.4, with some phase shift at different wave directions,

5.7 Conclusion

From this chapter, the hydrodynamic responses caused solely by first order wave loads are studied. Eignevalues of motions for the structure at each degree of freedom are obtained and compared with wave spectrum and 1P/3P frequencies from the turbines. The comparison indicates that extreme resonance will not take place for this design.

The responses are also calculated and analyzed. The results are converged and quite physical.

CHAPTER 6

Second Order Frequency Domain Analysis

6.1 Second Order Floater Hydrodynamics

Compare to the linear wave analysis, the second order frequency domain analysis takes into account the wave forces an order higher, which gives more accurate results. Especially, the drift forces can be described by the second order forces.

The governing equation can be written as,

$$(\mathbf{M}+\mathbf{A}(\omega))\ddot{\eta}+(\mathbf{B}(\omega)+\mathbf{D_1})\dot{\eta}+\mathbf{C}\eta=\mathbf{F}_w^{(1)}+\mathbf{F}_w^{(2)} \tag{6.1}$$

where $\mathbf{F}_w^{(1)}$ is the first order wave loads and $\mathbf{F}_w^{(2)}$ is the second order wave loads.

The second order quadratic forces may also contribute to the excitation at low or high frequencies other than wave frequencies. For the designed structure, it is of interest to predict the slow varying roll and pitch loads.

Practically, HydroD solves Eq. (6.1) by a separation of motion: the total motion response η is separated into a wave frequency component η_{WF} and a low frequency component η_{LF}, such that

$$\eta = \eta_{WF} + \eta_{LF} \tag{6.2}$$

The wave frequency force is caused by the first order wave loads with wave frequency, while as the low frequency force is excited by the second order wave loads with wave difference-frequency. Following this, the governing equation (6.1) is separated as,

$$\begin{cases} (\mathbf{M}+\mathbf{A}(\omega))\ddot{\eta}_{WF} + (\mathbf{B}(\omega)+\mathbf{D}_1)\dot{\eta}_{WF} + \mathbf{C}\eta_{WF} = \mathbf{F}_w^{(1)} \\ (\mathbf{M}+\mathbf{A}(\omega=0))\ddot{\eta}_{LF} + \mathbf{D}_1\dot{\eta}_{LF} + \mathbf{D}_2\dot{\eta}_{LF}|\dot{\eta}_{LF}| + \mathbf{C}\eta_{LF} = \mathbf{F}_w^{(2)} \end{cases} \tag{6.3}$$

It should be noted that the first equation in (6.3) is exactly the same as the first order motion equation. Hence in this chapter, the equation to be solved is the second equation in (6.3).

However, it should also be borne in mind that very little wave energy at low frequency is present in the ocean. Thus, even if the amplitude of transfer function might be high, slow varying responses caused by the waves should be less significant than the first order responses.

6.1.1 Second Order Hydrodynamic Force

The quadratic hydrodynamic forces can be obtained by integrating the pressure over the instantaneous wetted surface, as similar to the first order. The difference is the pressure is expressed to $O(\epsilon^2)$ by the second order potential flow theory as shown in section 2.2.2.

$$F = \oint_S p\mathbf{n}\,ds \tag{6.4}$$

where the vector **n** is pointing inside of the body and the 2^{nd} order pressure is expressed as

$$p = -\rho g z - \rho\frac{\partial\phi^{(1)}}{\partial t} - \rho\frac{\partial\phi^{(2)}}{\partial t} - \frac{1}{2}\rho\bigtriangledown\phi^{(1)}\cdot\bigtriangledown\phi^{(1)} \tag{6.5}$$

More specifically, dividing the wetted surface S into a constant area S_{0B} and a dynamic area, the low frequency second order force can be written as a summation of five different components after some mathematical simplification,

$$\begin{aligned}\mathbf{F} = &\underbrace{-\int_{WL}\frac{1}{2}\rho g(\xi_r^{(1)})^2\cdot\mathbf{n}\cdot dL}_{\text{I}}\underbrace{-\iint_{S_{0B}}\frac{1}{2}\rho|\nabla\phi^{(1)}|^2\cdot\mathbf{n}\cdot dS}_{\text{II}}\underbrace{-\iint_{S_{0B}}\rho\eta^{(\mathbf{1})}\cdot\nabla\frac{\partial\phi^{(1)}}{\partial t}\cdot\mathbf{n}\cdot dS}_{\text{III}} \\ &\underbrace{-\mathbf{M}\cdot\ddot{\eta}_G^{(1)}\times\alpha^{(1)}}_{\text{IV}}\underbrace{-\iint_{S_{0B}}\rho\frac{\partial\phi^{(2)}}{\partial t}\cdot\mathbf{n}\cdot dS}_{\text{V}}\end{aligned} \tag{6.6}$$

where,

(I) is the first order wave amplitude

(II) is the pressure change due to first order velocity

(III) is the pressure change due to product of first order pressure gradient and first order motion

(IV) is the pressure change due to first order moment of inertia and angular motions

(V) is the pressure change introduced by the second order velocity potential

Among the 5 terms, (I) - (IV) represent the quadratic contributions of the first order solutions, which are easily obtained from the first order solutions. The challenge lies in the term (V), the contribution from second order velocity potential.

To numerically solve for this second order velocity potential in term (V), a free water surface integral is needed in addition to the structure body mesh. The mathematical background is documented in WAMIT users' manual [25].

6.1.2 Transfer Function in Second Order

With irregular waves in cosine shapes, the slow drift loads in the designed semi-submersibles are mainly aroused by the difference-frequency effects. Neglecting the sum frequency effect, the force represented by equation (6.6) could be written in the form

$$F_j^{(2)} = \sum_{m=1}^{N}\sum_{n=1}^{N} A_m A_n\Big[T_{mn}^{jc}cos[(\omega_m-\omega_n)t+(\varepsilon_m-\varepsilon_n)] + T_{mn}^{js}sin[(\omega_m-\omega_n)t+(\varepsilon_m-\varepsilon_n)\Big] \tag{6.7}$$

where $A_m = \sqrt{2S(\omega_m)\Delta\omega}$, an amplitude that follows the wave spectrum $S(\omega)$ under the specific sea state. T_{mn}^{jc} and T_{mn}^{js} are the second order transfer functions for the difference frequency loads. These transfer functions are independent of the wave amplitudes, but are functions of

ω_m and ω_n. j refers to the degree of freedom.

Assuming two incident deep-water regular waves propagating in x direction

$$\begin{cases} \eta_1 = A_1 cos(\omega_1 t - k_1 x) \\ \eta_2 = A_2 cos(\omega_2 t - k_2 x) \end{cases} \tag{6.8}$$

Inserting equation (6.8) into equation (6.7), with $N = 2$, it is obtained that

$$F_j^{(2)} = \underbrace{A_1^2 T_{11}^{jc} + A_2^2 T_{22}^{jc}}_{\text{mean drift force}} + \underbrace{A_1 A_2[(T_{12}^{jc} + T_{21}^{jc})cos(\omega_2 - \omega_1)t + (T_{12}^{js} - T_{21}^{js})sin(\omega_2 - \omega_1)t]}_{\text{slow drift force}} \tag{6.9}$$

It is seen clearly that Eq. (6.9) consists of two parts: the mean drift force as a constant and the slow drift force as a sinusoidal varying term with the frequency $(\omega_2 - \omega_1)$. The mean drift force is not a function of wave frequencies, but governed by the first order transfer function $T_{11}^j s$ and $T_{22}^j s$, while the slow drift force is governed by the second order transfer function.

Due to the difficulty of calculating T_{mn}^{jc} and T_{mn}^{js}, Newman's approximation [30] is usually adopted for simplifying equation (6.7). It is assumed that

$$\begin{cases} T_{mn}^{jc} = T_{nm}^{jc} = \frac{1}{2}(T_{mm}^{jc} + T_{nn}^{jc}) \\ T_{mn}^{js} = -T_{nm}^{js} = 0 \end{cases} \tag{6.10}$$

Using Newman's approximation (6.10) by substituting arithmetic average with geometric average, the second order forces can be simplified to a function of only mean drift transfer function,

$$F_j^{(2)} \approx 2\Big[\sum_{m=1}^{N} A_m \sqrt{T_{mm}^{jc}} cos(\omega_m t + \varepsilon_m)\Big]^2 \tag{6.11}$$

It should be noted that Newman's approximation is valid only if ω_m and ω_n are fairly close, in other words, a small difference frequency condition. It is a good estimation for horizontal motions of a deep water offshore structure in our case.

Second order difference frequency behavior, namely the slow drift force term, can be interpreted from the second order transfer function T_{mn}^{jc}.

6.2 Calculation Method

There are two ways supported by HydroD to estimate the mean drift forces: direct pressure integration and conservation of fluid momentum. Brief introduction of the fundamentals is demonstrated. Chang-Ho Lee [26] compared these two methods on a hemisphere and a cylinder geometry.

Direct pressure integration(DPI) is the integration of fluid pressure over the instantaneous wetted surface, as shown in Eq. (6.4).

6.2.1 Conservation of Fluid Momentum(CFM)

In the CFM method, the forces are obtained by solving the equation of fluid moment conservation inside a fluid control volume Ω:

$$\frac{d}{dt}\Big(\int_{\Omega} \rho \mathbf{V}\, d\Omega\Big) = \mathbf{F}_s + \mathbf{F}_v - \int_{S} \rho \mathbf{V}(V_n - U_n)\, dS \tag{6.12}$$

This equation means the time variation of the fluid momentum inside the volume equals to the sum of the surface forces acting on its enclosing surface($\mathbf{F}_s$), the volume forces acting on the enclosed volume($\mathbf{F}_v$) and the net flux of fluid momentum through its enclosing surface($-\int_S \rho \mathbf{V}(V_n - U_n)\, dS$).

6.2.2 Comparison between DPI and CFM

When the mean drift forces are of interest, equation (6.12) might be simplified to an integral on a far-field control surface, which provides more accurate results than DPI. However, the momentum conservation equations can only be established for horizontal mean drift forces and vertical moments.

Pressure integration, on the other hand, is straightforward and can be done for all degrees of freedom. Nevertheless, it is reported that DPI involves different terms which counteract each other when the force component at a single degree of freedom is to be extracted [14]. This could cause accuracy concerns.

CFM results are generally more accurate but only applicable for limited force and moment components.

It should be noted that the computational result of the quadratic pressure forces is generally less accurate than the first order forces. Thus it demands significantly more refined descretization and increased computing time.

To obtain a reasonable results of QTFs (generated by DPI method) for time domain simulation, the results of mean drift force from DPI is compared with results from CFM to ensure the reliability of the results. On the other hand, a mesh convergence study is also carried out.

6.3 Meshing

In order to estimate the second order velocity loads, a free surface mesh together with the panel model mesh are required.

A challenge here is to generate the difference frequency quadratic transfer function(QTF). Due to the delicacy of the higher order calculation, resolution of second order terms are much more sensitive to the mesh quality and thus a mesh convergence study is done carefully to ensure a valid results.

HydroD uses the WADAM solver to compute the second order forces [15]. A specific limit is that the number of free surface panels should be less than 6000.

6.3.1 Free Surface Mesh

Free Surface Mesh required by HydroD has to be a circle. Due to x-z symmetry of the structure, half of the model is built. Hydro user's manual [16] empirically specified the radius of the surface mesh to be larger than the water depth. Therefore, The radius of the surface mesh is set to 300m.

To eliminate the triangular elements on the surface mesh, the whole surface is divided into multiple blocks and each side of the blocks is controlled by feature edges, on which the element seeds are manually controlled.

After trial and error, two layers of feature edges close to each column are designed for a good mesh quality around the contact areas of water surface and the structure. Four diagonal feature edges around the holes are also used to obtain quadrilateral elements, demonstrated in figure 6.2a. A good mesh quality around the columns are finally obtained as shown in figure 6.2b.

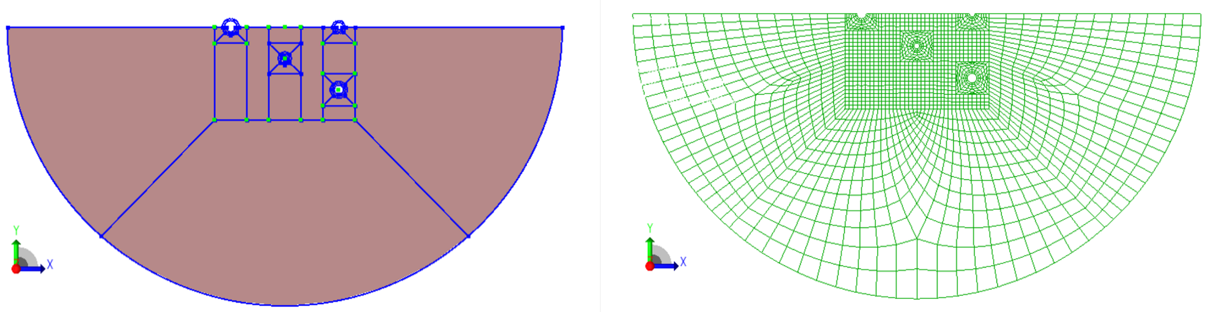

(a) Block Division of the Surface

(b) Mesh of the 1/2 free surface model

Figure 6.1: Water Surface

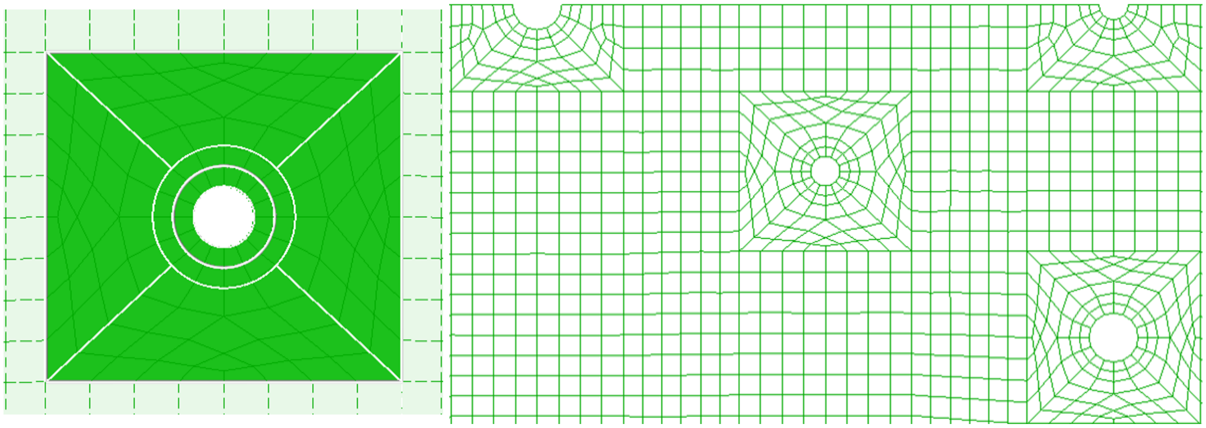

(a)

(b)

Figure 6.2: Mesh details around the columns

After implementing block divisions and feature edges, the water surface in figure 6.1a is turned into a mesh illustrated as figure 6.1b.

6.3.2 Panel Model Mesh

The meshes for the semi-submersible is also re-designed to exactly match the nodes of the free surface at water line. In practice, some feature edges are employed again on the submerged parts. Several meshes with different element size of the model are also designed from $2m \times 2m$ to $1m \times 1m$. It is observed that the mesh density of submerged part is of great significance to the second order force calculation, which is demonstrated in Chapter 6.3.3 Mesh Convergence Study.

6.3.3 Mesh Convergence Study

Three meshes listed in Tab. 6.2 are designed and compared. Above all, the impact from free surface mesh quality is examined by comparing the results from Mesh 1 and Mesh 2. Compared to Mesh 1, a prominent improvement of surface mesh density is employed in Mesh 2, especially on the area around the columns. The mesh of the panel model remains the same, with a mesh size of $2m \times 2m$. Mesh 3 is designed to examine the influence from the panel model mesh quality. Comparing Mesh 2 and Mesh 3, the element number on the submerged body is increased dramatically.

Table 6.1: Mesh for the convergence study

	Element Number on surface	**Element Number on structure**
Mesh 1	3848	2844
Mesh 2	5752	2844
Mesh 3	5752	7784

Mean drift forces as a function of wave frequency are compared. Results presented are under the wave direction 0°. Figure 6.3 shows the mean drift forces of all three meshes by the CFM method.

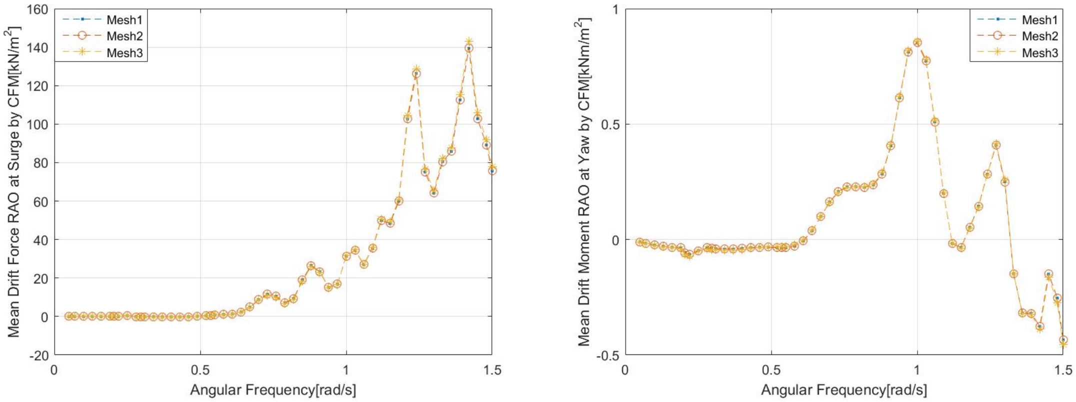

Figure 6.3: CFM Result Comparison

It is seen clearly that results by CFM method from the three meshes are well converged. The agreement between Mesh 1 and Mesh 3 also demonstrates the superiority of the accuracy provided by CFM method in terms of low mesh density requirement. It might be safe to take

CFM results as reference to evaluate the accuracy of results from DPI method, which are shown in figure 6.4.

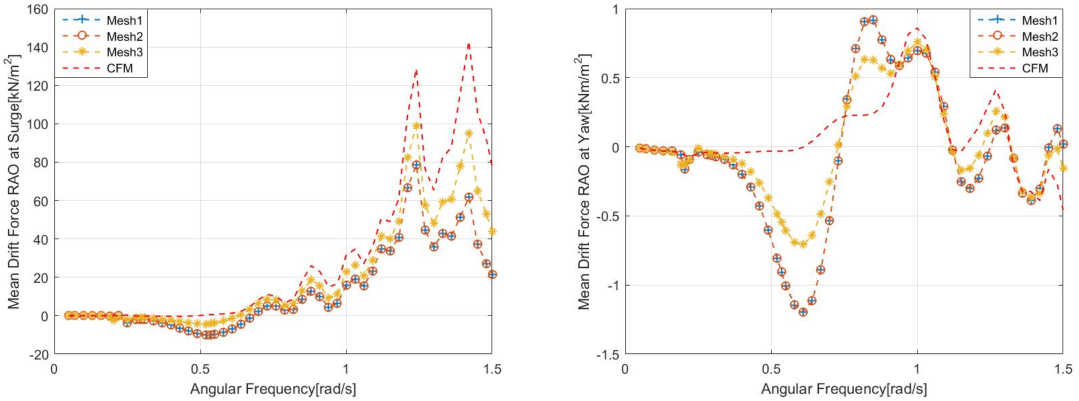

Figure 6.4: Mean Drift Force Comparison

From figure 6.4, it can be seen that the difference between Mesh 1 and Mesh 2 are very limited and the results from Mesh 3 are the closest to the CFM method. This indicates the high mesh density on the panel model is more important for the accuracy of second order results.

6.3.4 Final Mesh

It might be concluded that a coarse surface mesh used in Mesh1 is satisfactory in the calculation because little difference between Mesh1 and Mesh2 is observed in both mean drift forces and quadratic transfer function. It is also seen that a fine mesh on the submerged structure is desirable for more accurate result.

The final mesh is designed to have the same surface mesh as Mesh1 but with a very fine structure mesh as affordable as possible, demonstrated in figure 6.5a.

Table 6.2: Final Mesh

	Element Number on surface	**Element Number on structure**
Final Mesh	3848	8418

Fig 6.5b shows a good agreement between DPI and CFM in the surge mean drift force tendency. However, it is also observed that deviation of the two curves becomes significant at

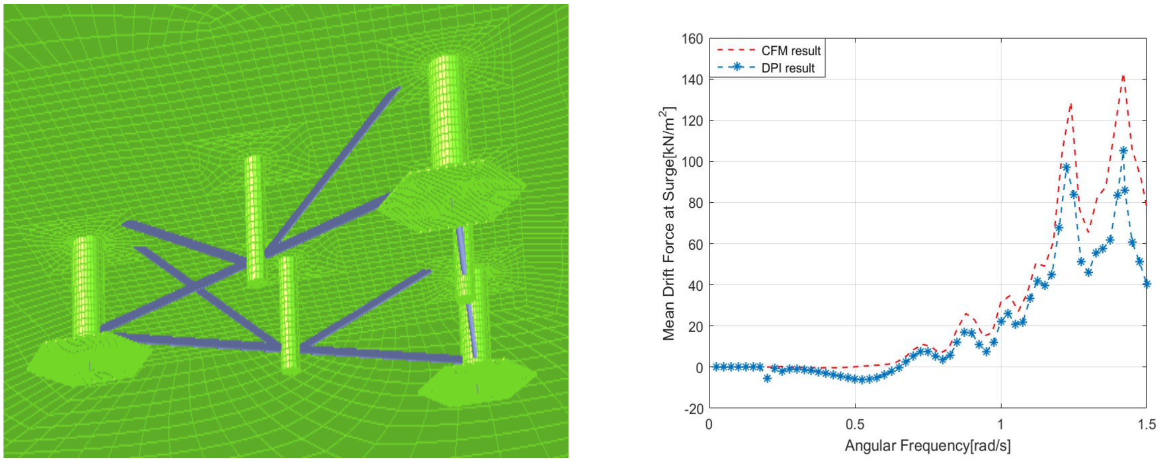

(a) Bottom View of the Final Mesh

(b) DPI vs CFM in surge

Figure 6.5: The final mesh and its results

higher frequencies. Better quality mesh could have been used, but the calculation will be very time consuming. The result from the final mesh is a good compromise and therefore adopted as a valid results for second order analysis.

6.4 Result & Analysis

The second order forces results are focused on surge, sway and yaw, where the mooring line system is supposed to provide the stiffness in the motion equation. Pitch is also of interest because wind turbine is vulnerable at this DOF. The second order results are examined also under the extreme condition.

From equation (6.9), it is seen clearly that the second order wave forces consists of a mean component and a slow varying component, which is governed by second order transfer function. These two parts of the designed semi-submersible wind turbine are presented and discussed below.

6.4.1 Asymptotic Value

Before looking at the results from HydroD, an analytical asymptotic value is presented, which helps to understand the behavior of the mean drift forces.

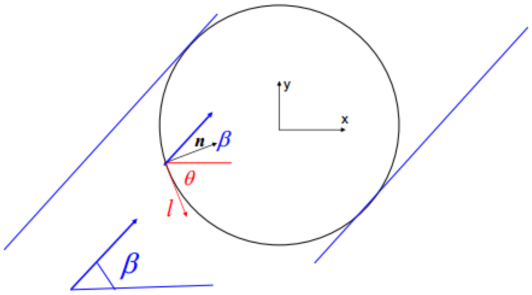

Figure 6.6: diagram of a cylinder

The mean drift forces are associated with the body's ability to generate waves. When frequencies are low and waves are long, the structure tends to follow the waves. Under this scenario, the first order motions are significant and diffraction effects become less insignificant and mean drift forces are close to zero. In other words, the mean drift forces are notable at higher frequencies.

When $\omega \to \infty$, the waves are completely reflected and the mean drift force reaches its asymptotic value at this point.

A extend Maruo's formula can be employed to calculate this asymptotic value of the vertical cylinders in water [31]. This formula is valid for horizontal forces and yaw forces.

$$\bar{F}_i^{(2)} = \tfrac{1}{2}\rho g \xi_a^2 \int_L [sin(\theta+\beta)]^2 n_i \, dl \quad i = 1,2,6 \tag{6.13}$$

where ξ_a is the incident wave height.

At surge and sway, the maximum mean drift force in case of a cylinder with radius r is,

$$\bar{F}_i^{(2)} = \tfrac{2}{3}\rho g r \xi_a^2 \quad i = 1,2 \tag{6.14}$$

Specifically, in the case of this structure, there are 6 columns taken into account, with radius 5m and 3m. The analytical solution to this problem would become, considering a unit wave height $\xi_a = 1m$

$$\bar{F}^{(2)} = \frac{2}{3}\rho g r \xi_a^2 = \frac{2}{3} \times 1025 \times 9.81 \times (5+3) \times 3 \times 1^2 = 160[kN] \tag{6.15}$$

From the calculation above, it can be estimated that the mean drift forces at surge and sway will generally becomes higher as frequency increases and $\frac{\bar{F}^{(2)}}{\xi_a^2} \rightarrow 160kN/m^2$ when $\omega \rightarrow \infty$.

6.4.2 Mean Drift Force

Figure 6.7 shows the mean drift force transfer function, the amplitude of which can be expressed as $\frac{\bar{F}^{(2)}}{\xi_a^2}$.

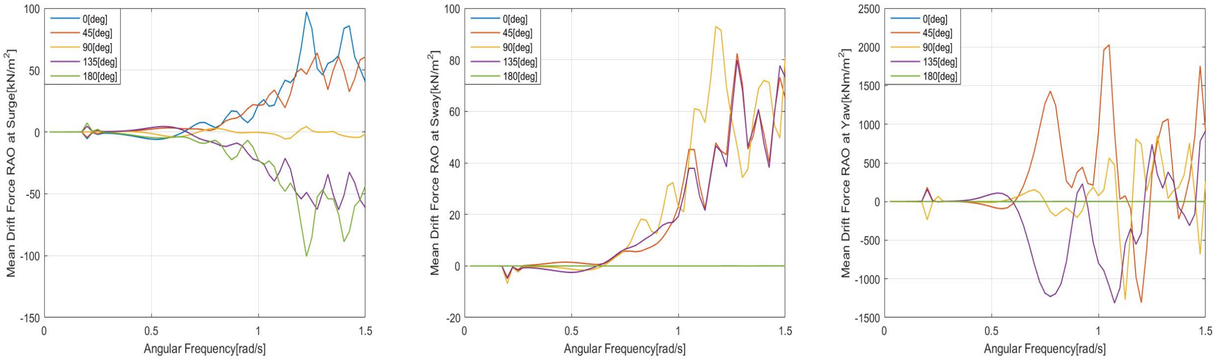

(a) Surge (b) Sway (c) Yaw

Figure 6.7: Mean Drift Force amplitude as a Function of Wave Frequency

Generally, it can be observed that mean drift forces become more significant for higher wave frequencies($\omega > 1 rad/s$). At surge and heave, the maximum amplitude value is around $100kN/m^2$. It should be noted that the results from DPI method are less accurate. The real value might be higher as illustrated in fig 6.5b. But the mean drift forces at surge and sway match with the asymptotic value prediction.

From figure 6.7a, it is observed that there are small peaks at $\omega \approx 0.2 rad/s$, which is the eigenfrequency of the surge motion. It can also be seen that the force amplitudes are almost symmetric about $y = 0$ for the wave incident angle $\theta = 0°$ and $\theta = 180°$, $\theta = 45°$ and $\theta = 135°$. The maximum value happens at head sea and following sea. At the beam sea situation, second order force at surge is oscillating around 0, this disturbance comes the asymmetry at $y - z$ plane.

Mean drift forces at sway are demonstrated in fig 6.7b, when $\theta = 0°$ and $180°$, there is almost zero, due to the symmetry at $x - z$ plane. The maximum mean drift force at sway take place when $\theta = 90°$ and in the same order of surge forces. The yaw mean drift transfer function amplitude is much higher compared to the ones at surge and sway. This is because the large size of the platform in the horizontal plane.

Fig 6.7 shows the maximum mean drift force at surge happens when $\theta = 0°$, maximum mean drift force at sway happens when $\theta = 90°$ and the maximum mean drift force at yaw happens at $\theta = 45°$. A comparison is performed between second order mean drift forces and the first order force RAO at the most severe wave directions. Figure 6.8 demonstrates the comparison.

It is found that the maximum linear wave excitation forces to be about $10^3\xi_a(kN)-10^4\xi_a(kN)$ while the horizontal mean drift force is about $10^2\xi_a^2(kN)$. This means for a wave amplitude of $1m$, the linear wave excitation forces are 50 times larger; for a wave amplitude of $10m$, the first-order forces are about 10 times larger.

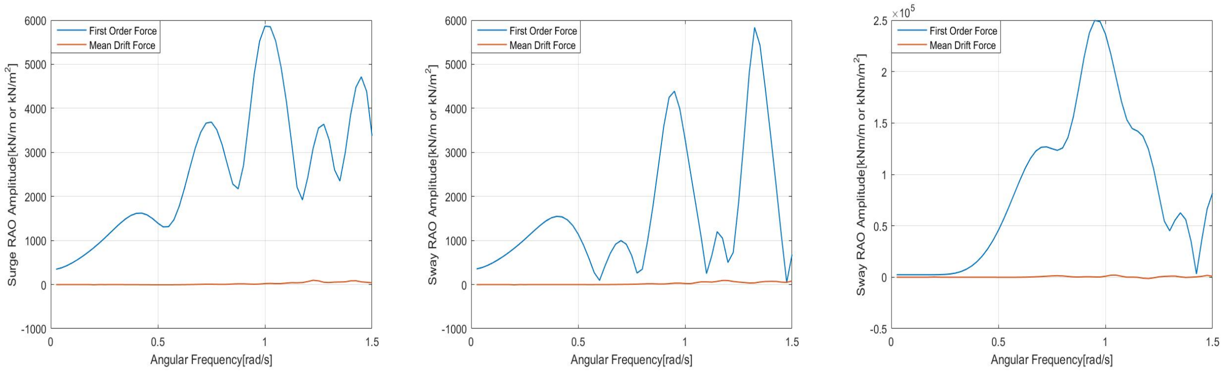

(a) Surge at $\theta = 0°$ (b) Sway at $\theta = 90°$ (c) Yaw at $\theta = 45°$

Figure 6.8: Comparison between first order force and mean drift force amplitude

6.4.3 Quadratic Transfer Function

Equation (6.9) indicates that the slow drift force component is determined by the quadratic transfer function T_{mn}. By definition, diagonal values of the QTF is T_{mm}, which is the mean drift transfer function.

Figure 6.9 shows the QTF at surge, yaw and pitch. The white dashed lines demonstrate the diagonal terms where $\omega_m = \omega_n$. It can be seen that the QTF value tends to be higher for off diagonal frequencies. This is because the slow drift effect becomes more pronounced when the frequency difference increases. Looking at the pitch QTF in Fig. 6.9c, the QTF value changes quickly around the natural frequencies and also the peaks of first order forces. Note that the mooring system is not considered in the model yet and therefore the eigenfrequencies at horizontal dofs are still zero, which could be a source of inaccuracy.

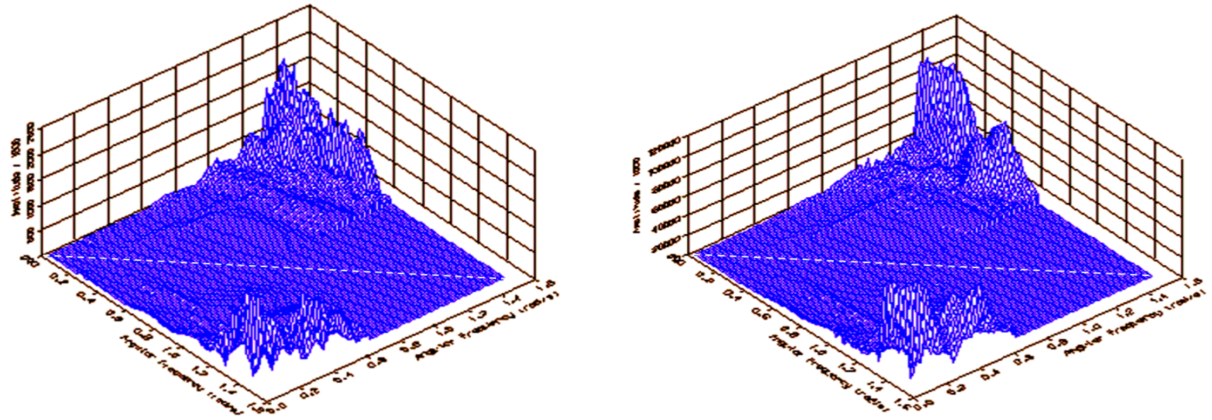

(a) Surge at $\theta = 0°$

(b) Yaw at $\theta = 45°$

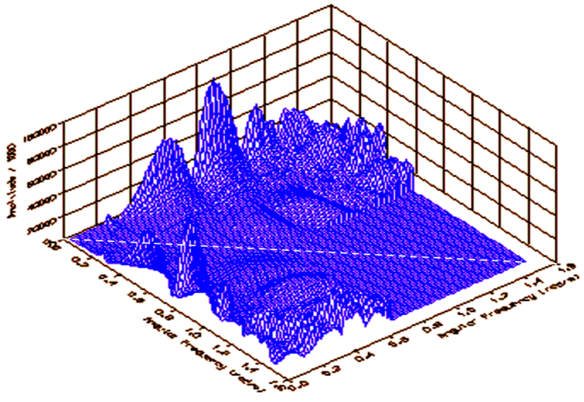

(c) Pitch at $\theta = 0°$

Figure 6.9: second order transfer function amplitude as a function of wave frequency

Additionally, it can be interpreted from Fig 6.9 that difference frequency terms might have slight influence on standard deviation of the responses due to its low frequency, but it might effect the mean value dramatically because of the large amplitude difference between diagonal values and off diagonal ones.

6.5 Conclusion

Second order forces are less significant compared to the first order forces. For an offshore structure, the results are sensitive to wave heading, body motion, wavelength and wave height.

In general, mean drift force result into the mean value in motion responses. Second order slow varying force could become fairly large and hence might be inevitable for mooring design and structural strength but does not contribute significantly to the structure fatigue.

CHAPTER 7

Mooring and Anchor Systems

So far, all the analysis has been carried out in the frequency domain without mooring system.

The mooring system, however, is designed to counteract the mean drift loads due to waves, current and wind and also provides a damping and restoring force at the horizontal motions, i.e. surge, sway and yaw motions, which do not have any hydrostatic restoring stiffness.

Thus the mooring cables with effective stiffness, partially elastic and partially geometric, result into the restoring force due to the anchor-line tension, i.e. $K_{11}\eta_1 = \left(\frac{dT_H}{dx}\right)|_{x=x_{mean}}\eta_1$. They also contribute in terms of slow-drift damping to the system, which is a viscous damping, e.g. the damping force in surge can be expressed as $B_{11}\dot{\eta}_1|\dot{\eta}_1|$. Generally, the governing equation of motion, taking into account the mooring line stiffness **K**, can be expressed as,

$$(\mathbf{M}+\mathbf{A}(\omega))\ddot{\eta}+(\mathbf{B}(\omega)+\mathbf{D_1})\dot{\eta}+(\mathbf{C}+\mathbf{K})\eta=\mathbf{F}_w^{(1)}+\mathbf{F}_w^{(2)} \tag{7.1}$$

Referring to the DNV-OS-E31 [3], the effects of mooring system can be summarized as

1. Weight Effect

   Mooring system can induce static vertical loads (downwards) on the platform due to weight (or pre-tension) of the lines.

2. Stiffness Effect

   Provide the stiffness for surge, sway and yaw motions by providing **K**,

$$T = 2\pi\sqrt{\frac{\mathbf{M}+\mathbf{A}}{\mathbf{K}}} \tag{7.2}$$

3. Damping Effect

   Drag force on mooring lines will give the damping effect on the platform motions, especially the slowly-varying motions.

Major conclusions of the mooring lines static analysis are listed and a preliminary mooring line design is performed. In this design, only linear mooring forces are considered. Details can be found in *Sea Loads on Ships and Offshore Structures* [31].

7.1 The Catenary Theory

7.1.1 Single Catenary Chain

Mooring lines are made of sets of cables connecting the vessel to the sea floor (either laying or attached to the sea floor). A pre-tension is applied to keep the lines in place. System motions consequent to the environmental conditions modifies the geometry and tension of lines. Figure 7.1a [5] shows the general situation of the single catenary line and figure 7.1b [5] demonstrates a static analysis diagram of a cut-out part of it.

The static equilibrium in figure 7.1b can be established tangentially and normally as,

$$\begin{cases} dT - \rho g A dz = [w sin\phi - F(1 + T/(AE))]ds \\ T d\phi - \rho g A z d\phi = [w cos\phi + D(1 + T/(AE))]ds \end{cases} \tag{7.3}$$

where $w[N/m]$ is the weight per unit for the catenary line. A is the cross section area. The water pressure on cross sections $\rho g A z$ and $(\rho g A z - \rho g A)$ at the ends are included as hydrostatic corrections.

Catenary equations (7.3) can be solved using the boundary conditions at the fairlead and at the anchor positions, which gives the cable configuration as,

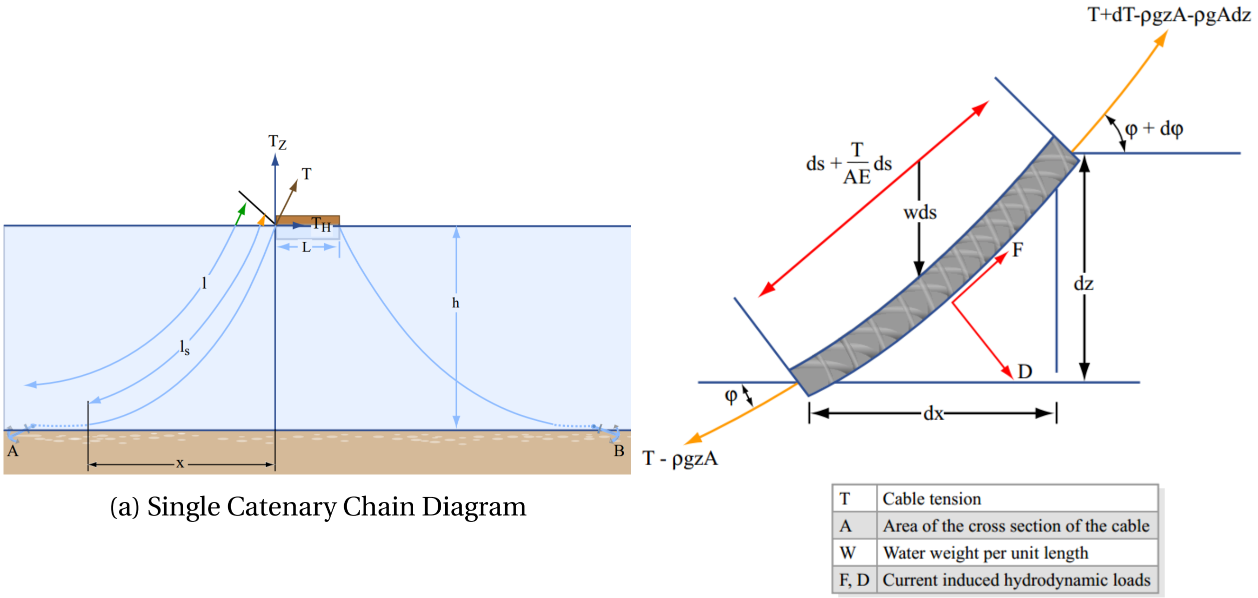

T	Cable tension
A	Area of the cross section of the cable
W	Water weight per unit length
F, D	Current induced hydrodynamic loads

(a) Single Catenary Chain Diagram

(b) Static Analysis of Single Catenary Chain

Figure 7.1: Single Mooring Line

$$\begin{cases} s = \frac{T_H}{w} sinh\left(\frac{w}{T_H}x\right) \\ z + h = \frac{T_H}{w}\left[cosh\left(\frac{w}{T_H}x\right) - 1\right] \end{cases} \tag{7.4}$$

Tension along the cable can be expressed as

$$\begin{cases} T = T_H + wh + (w + \rho g A)z \\ T_z = ws \end{cases} \tag{7.5}$$

The minimum line length required for a gravity anchor,

$$l_{min} = h\sqrt{\frac{2T_{max}}{wh} - 1} \tag{7.6}$$

The horizontal force for a given fairlead tension,

$$T_H = T - wh \tag{7.7}$$

The horizontal scope from the fairlead to the touchdown point,

$$x = \frac{T_H}{w} sinh^{-1}\Big(\frac{wl_{min}}{T_H}\Big) \tag{7.8}$$

The vertical force at the fairlead,

$$T_z = wl_{min} \tag{7.9}$$

The horizontal distance from fairlead to the anchor is $X = l - l_s + x$, inserting all the terms, X can be expressed explicitly as,

$$X = l - h\sqrt{1 + 2\frac{T_H}{wh}} + \frac{T_H}{w} cosh^{-1}\Big(1 + \frac{wh}{T_H}\Big) \tag{7.10}$$

Therefore, as a characteristic for stiffness, the restoring coefficient becomes,

$$C_{11} = \frac{\Delta F_x}{\Delta x} = \frac{dT_H}{dX} = w\Bigg(\frac{-2}{\big(1 + 2\frac{T_H}{wh}\big)^{1/2} + cosh^{-1}\big(1 + \frac{wh}{T_H}\big)}\Bigg)^{-1} \tag{7.11}$$

7.1.2 Catenary Mooring System

Figure 7.2 shows a sketch of a rigid body connected to multiple mooring lines. The system can be considered as a sum of every single mooring line presented in section 7.1, transferring from a local coordinate to the global coordinate. The DOFs of interest are surge, sway and yaw.

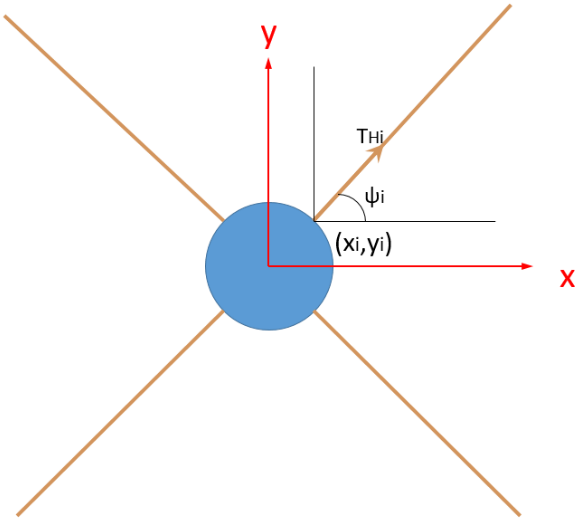

Figure 7.2: Example of the Mooring System

Under the global coordinate, the forces from turret mooring system can be described as,

$$\begin{cases} F_1^M = \sum_{i=1}^n T_{Hi} cos\psi_i \\ F_2^M = \sum_{i=1}^n T_{Hi} sin\psi_i \\ F_6^M = \sum_{i=1}^n T_{Hi}(x_i sin\psi_i - y_i cos\psi_i) \end{cases} \tag{7.12}$$

where T_{Hi} is the horizontal force from mooring chain number i.

Similarly, the linear restoring effect of the turret system can be expressed as a sum of each mooring line. It can be found in equation (7.11) that there is no coupling effect between surge and other two horizontal DOFs when the mooring management is x-z symmetric, in another word, $C_{12} = C_{21} = C_{16} = C_{61} = 0$. The remaining restoring coefficient of a global manner becomes,

$$\begin{cases} C_{11} = \sum_{i=1}^n k_i cos^2\psi_i \\ C_{22} = \sum_{i=1}^n k_i sin^2\psi_i \\ C_{66} = \sum_{i=1}^n k_i (x_i sin\psi_i - y_i cos\psi_i)^2 \\ C_{26} = C_{62} = \sum_{i=1}^n k_i (x_i sin\psi_i - y_i cos\psi_i) sin\psi_i \end{cases} \tag{7.13}$$

where k_i is the restoring coefficient for mooring line i.

7.2 Design Requirement and Procedure of Mooring System

General requirements for mooring lines are

Stiffness requirement. The stiffness of the mooring system should be adequate to keep the offset of the platform such that there is no vertical forces on any anchor. The mooring system also need to provide stiffness to justify the natural frequencies of horizontal motions.

Strength requirement. The mooring system should be strong enough to maintain its structural integrity. Specifically the maximum tension each mooring line subjected to should not exceed its breaking strength.

The following steps are performed to complete a mooring line design:

1. The natural periods at all degrees of freedom should be longer than 25s in order to avoid first-order wave excitation. The decoupled undamped natural period can be simply estimated from

$$T_j = 2\pi\sqrt{\frac{M_j + A_j}{C_j + K_j}}$$

2. The mean offset is a function of the mooring system stiffness and the mean load due to wind, waves, and current. In this preliminary design, the wind effect is taken to be the maximum steady turbine thrust, the mean surge force due to waves $\bar{F}_1$ is estimated from the pressure integration and viscous forces as in Eq. (7.14),

$$\bar{F}_1 = \frac{2}{3}\rho g \xi_a^2 \frac{D}{2} + \frac{2}{3\pi}\rho C_D D \omega^2 \xi_a^3 \tag{7.14}$$

   where ξ_a is the wave significant amplitude. $\frac{2}{3\pi}\rho C_D D\omega^2\xi_a^3$ represents the drift force created by viscous drag. More details about the viscous drag are elaborated in [31].

   During the mooring design, the mean offset is estimated under the rated wind speed that corresponds to the maximum thrust. The drag coefficient $C_D = 1$. Current is neglected here.

3. The cross sectional area of the mooring line must be sufficient in terms of strength.

$$\frac{2F_t}{A_t} \leq \frac{\sigma_y}{SF} \tag{7.15}$$

Following the procedures above, the preliminary mooring line is designed.

7.3 Modelling of Mooring System

The mooring system is modelled in SIMA, considering the coupled dynamics of the mooring system together with the floater dynamic behavior. The geometry of the floater is replaced by a small rigid body with all the kinetic information, mass, damping, mean drift force transfer function etc. Mooring lines are modelled and connected to the ’rigid body’ with proper node connections and boundary conditions.

Table 7.1: Preliminary mooring system properties

Mooring line configuration	
Number of mooring lines	5[-]
Angel between adjacent lines	72 [deg]
Water depth	200[m]
Depth from fairlead to seabed	185[m]
Unstretched mooring line length	880[m]
Mooring line angle at fairlead	43[deg]
Chain type	Studless grade 3
Chain equivalent diameter	76.6[mm]
Mooring line unit mass in water	0.109[t/m]
Mooring line axial stiffness	8E+05[kN]
Transverse drag coefficient of mooring line	2.4[-]
Longitudinal drag coefficient of mooring line	1.15[-]
Transverse added mass coefficient of mooring line	2[-]
Longitudinal added mass coefficient of mooring line	1[-]

Through a static mooring analysis, it is found that the three-line Plan 1 shown at Fig. 7.3a cannot provide enough stiffness for yaw and a numerical divergence is reported by the software under rougher sea conditions. Therefore, the mooring system is adjusted to five mooring lines where the five lines are connected to two columns, as in fig 7.3b.

The mooring system inertia, structural elasticity, added mass and damping forces are all taken into account by modelling the mooring lines as fully nonlinear finite element model. The calculation is done in time domain and the governing euquation can be written as,

$$(\mathbf{M}+\mathbf{A}(\omega))\ddot{\eta}(t)+\mathbf{B}(\omega)\dot{\eta}(t)+(\mathbf{C}+\mathbf{K})\eta(t)=\mathbf{F}_w^{(1)}+\mathbf{F}_w^{(2)}-\mathbf{D_1}\dot{\eta}(t)-\mathbf{D_2}\dot{\eta}(t)|\dot{\eta}(t)| \tag{7.16}$$

7.4 Results

The results are examined under the extreme condition, where the hydrodynamic loads dominate and the turbines idle.

The calculated static initial positions are,

It is seen from Tab. 7.2 that the mooring system influence the floating state of the structure. Intuitively, the displacement at X direction comes from the mean drift force. The displacement

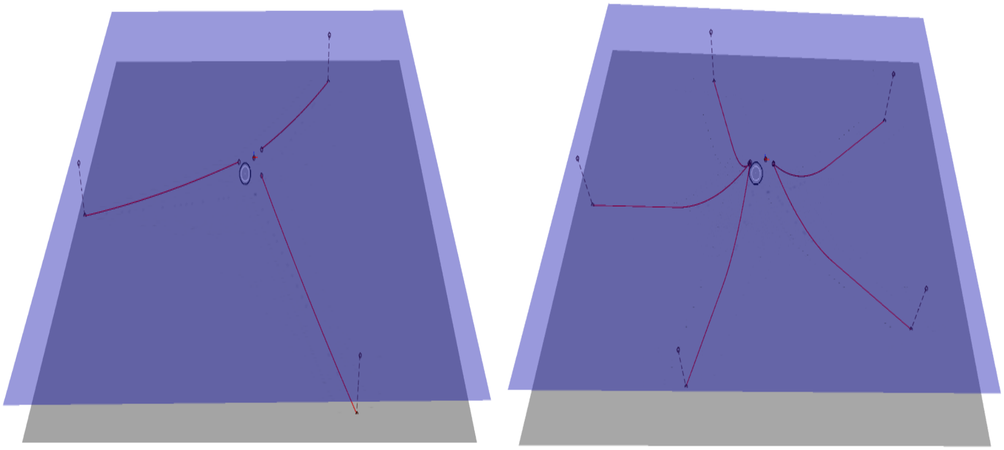
(a) Plan1 (b) Plan2

Figure 7.3: Mooring Arrangement

Table 7.2: Static Initial Position of the Structure

State	$X[m]$	$Y[m]$	$Z[m]$	$Rx[deg]$	$R_y[deg]$	$R_z[deg]$
Before Moored	0	0	0	0	0	0
After Moored	-1.22	0	-0.594	0	-0.519	0

at Z direction is due to extra mooring system weight. Angular displacement at R_y is the result from mooring line tension and mean drift force.

The mooring system, of course, will change the eigenfrequency at each direction. To determine the new eigenfrequency, time domain free decay test is normally required [3]. However, another method can also be used to roughly grasp the eigenfrequency of the moored platform, by spectrum analysis for different wave seeds.

Different wave seeds will initiate different instantaneous wave elevation of the same H_s and T_p. Therefore the response spectra from these waves are expected to have the same peak at eigenfrequencies.

Wave seeds 1-10 are implemented under the extreme condition, and the time domain responses are turned into frequency domain spectrum.

It is seen from Fig 7.5 that there are generally two peaks at Surge direction. The lower frequency should be the eigenfrequency at surge. The second one could be the quadratic terms such as quadratic damping.

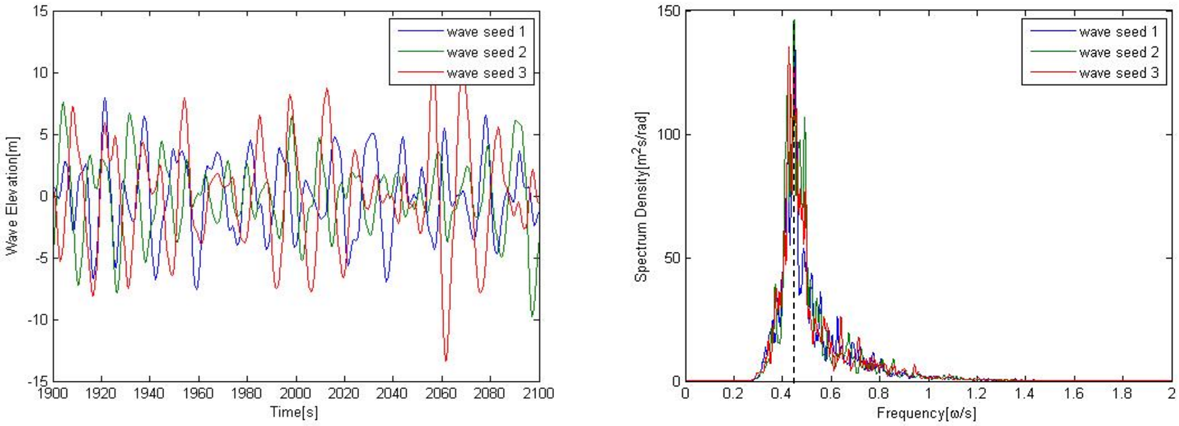

(a) Time Domain Wave Elevation (b) Wave Spectra

Figure 7.4: Illustration of different wave seeds

Table 7.3: Response at Surge Heave and Pitch

Wave Seed	**Mean Surge**[m]	**Mean Heave**[m]	**Mean Pitch**[°]
1	0.9725	0.5337	0.5154
2	1.4328	0.5262	0.5187
3	1.2032	0.5261	0.5186
4	0.8837	0.5346	0.5183
5	1.3428	0.5301	0.5128
6	1.1155	0.5306	0.5187
7	1.2779	0.5294	0.5196
8	1.0884	0.5331	0.5200
9	1.0332	0.5221	0.5181
10	1.0561	0.5265	0.5186

The heave motion shown in fig 7.5b is a bit strange because the heave motion does not follow the wave spectrum shown at fig 7.4b. From the frequency domain analysis done before, the heave and pitch eigenfrequencies are expected to be close to $0.25Hz$ and $0.2Hz$. Considering the small mean surge displacement and maximum mooring line tension in Tab 7.4, there might be some numerical error occurred in during the simulation.

It is also seen that the heave and pitch spectral density from different wave seeds does not agree very well. The peaks are expected to be around the same frequency.

The numerical divergence reported when the first mooring arrangement in fig 7.3a was tested should be treated more seriously. The true reason of the divergence should be understood and

Table 7.4: Maximum Mooring Line Tension

Wave Seed Number	**Line No.1** $[kN]$	**Line No.2** $[kN]$	**Line No.3** $[kN]$
1	567.96	571.38	603.39
2	562.89	569.82	613.59
3	567.38	571.59	609.89
4	571.24	571.45	601.07
5	562.92	569.50	611.65
6	565.46	570.72	607.25
7	564.33	570.27	608.25
8	568.57	571.04	608.78
9	571.14	572.05	608.88
10	568.04	571.40	607.27

a new mooring system should be re-designed.

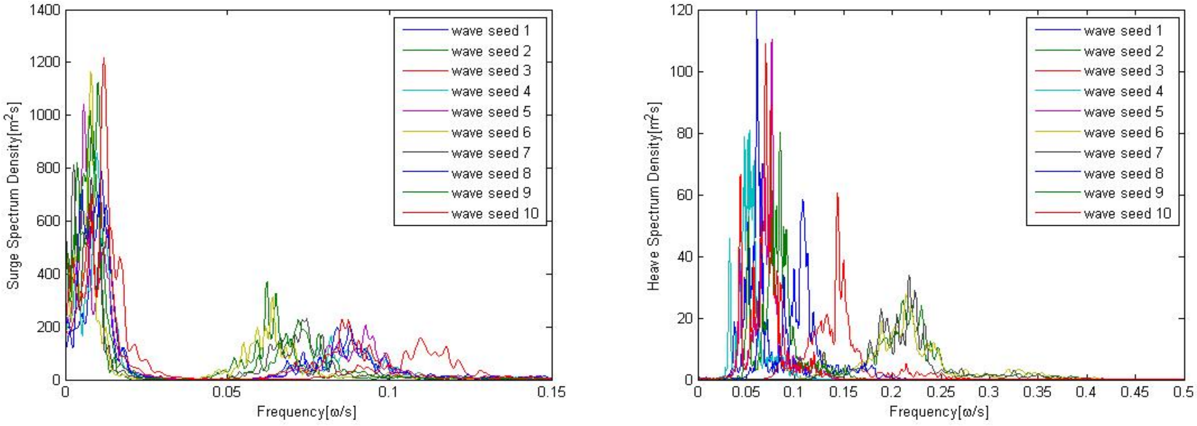

(a) Surge (b) Heave

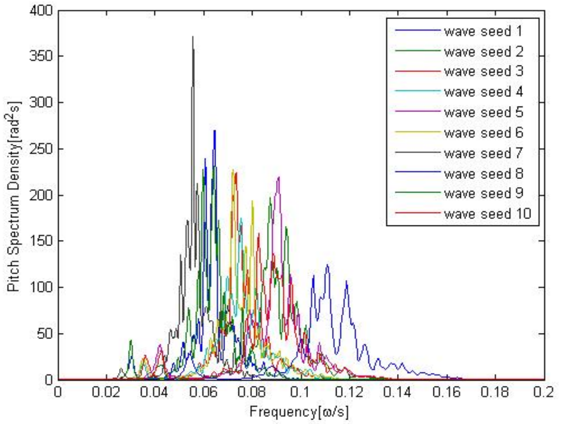

(c) Pitch

Figure 7.5: Spectral Density

CHAPTER 8

Time Domain Response Model

8.1 Multiple Turbine Time Domain Mathematical Model

In the last model, aerodynamic loads are included in the time domain equation,

$$(\mathbf{M}+\mathbf{A}(\omega))\ddot{\eta}(t)+\mathbf{B}(\omega)\dot{\eta}(t)+(\mathbf{C}+\mathbf{K})\eta(t) = \mathbf{F}_w^{(1)}+\mathbf{F}_w^{(2)}+F_{turbine}^{(1)}+F_{turbine}^{(2)}-\mathbf{D_1}\dot{\eta}(t)-\mathbf{D_2}\dot{\eta}(t)|\dot{\eta}(t)| \quad (8.1)$$

where $F_{turbine}^{(1)}$ is the wind loads from the first turbine and $F_{turbine}^{(2)}$ is the wind loads from the second turbine.

Because there are the two turbines with nonidentical instantaneous aerodynamic loads, each turbine force should be considered separately. This can be done by creating two interrelated wind profiles by changing the wind seed number.

As discussed earlier, the interaction between turbines are neglected. Therefore the coupling term between turbines might be set to zero. Two aerodynamic forces can be added as external forces on top of the hydrodynamic model in section 7.3.

During the process, the platform is treated as a rigid body in Simo-Riflex for simplicity; elasticity of the structure is not considered in the model. This is valid because the motions of floating wind turbines are dominated by rigid body motions rather than elastic deformations. [14]

8.2 Aerodynamic Load Simulation Tool

Various methods have been developed to calculate the aerodynamic loads, varying from a Blade Element Momentum method to Full Computational Fluid Dynamics method with different computational efforts and accuracy.

One of the most famous design code for turbine aerodynamics is Aerodyn, which is developed by NREL [22]. Y.H.Bae [37] expanded the Aerodyn code such that multiple wind turbines can be accounted.

Expanding the code for multiple turbines requires considerable time and efforts and out of the scope of this thesis. Therefore a full coupled time domain simulation is not performed in this master thesis. To solve the equation (8.1), the TDHMILL code is adopted instead, which is a aerodynamic simulator empirically implemented by Statoil. Theory background of the code is introduced in the section 2.3.

A through comparison between the coupled aero-hydro-servo-elastic time domain analysis and Simo-Riflex-TDHMILL3D time domain analysis for two spar type turbines is done by Madjid Karimirad [28]. High agreement is reported between this simplified method and the sophisticated method. Validation of TDHMILL code is also proven by many other project experiences from MARINTEK.

However, implementing TDHMILL also has several drawbacks:

- TDHMILL only takes into account the rotor aerodynamics by preset thrust coefficient. drag forces or moments from tower and blade are neglected.
- TDHMILL only returns the aerodynamic forces, no controller data or power information involved at all.

It should be noted that TDHMILL might be an acceptable tool only for turbine response analysis.

CHAPTER 9

Conclusion

An initial design of the semi-submersible platform supporting two NREL 5MW wind turbines is carried out, mooring system included.

Hydrodynamic behavior of the semi-submersible platform is studied in details, under the extreme condition.

Wind turbine responses from both hydrodynamic and aerodynamic loads are of interest in the study. Efforts have been done to try to run the calculation. Unfortunately, the aerodynamic forces have yet included in the model within the given time. However, a solution method is offered to simulate the response of the turbine responses.

Some conclusions on the first order forces, second order forces and mooring systems have been drawn. Conclusion of the first order results are discussed in the section 5.6 and the second order results are discussed in the section 6.4.

Mooring lines are tested under the extreme condition. The results, however, seems to be problematic because of the response frequency peaks are spread out and the mooring line tension is too small to be under the extreme condition. Details included in section 7.4

9.1 Future Work

Due to a limited time, the proposed time domain numerical solution SIMO-RIFLEX-TDHMILL is not performed yet in the thesis because of an unexpected version mismatch between SIMO and TDHMILL.

Possibilities are that the two turbine aerodynamic loads can be added by running the SIMO-RIFLEX-TDHMILL in a batch mode with matched software versions.

More efforts are needed to include the aerodynamic loads. The spectrum analysis of the SIMO-RIFLEX-TDHMILL results, in terms of platform motions and maximum mooring tension, should be very interesting.

Other deficiencies of the study include

- The primary design of the platform is not optimal. The design can be improved by a brief study on the major dimensions.
- Only one environment condition is examined in the study, which is the extreme condition. Other conditions should have been investigated. Especially the rated condition with maximum aerodynamic loads.
- A close study to the mooring system is also needed. After spectral analysis, it is found that the designed mooring system is of problem.
- The strength and fatigue study is excluded when structural design is performed.

Bibliography

[1] *European structural steel standard EN 10025.*

[2] (2007). Recommended practice dnv-rp-c205: Environmental conditions and environmental loads.

[3] (2010). Offshore standard dnv-os-e31 position mooring.

[4] (2011). E.on offshore wind engnergy factbook.

[5] (2011). Mit opencourse notes: Design of ocean systems, lecture 12.

[6] (2013). Deep water, a report by the european wind energy association.

[7] (2016). The concept of hexicon: http://www.hexicon.eu/.

[8] (2016). The concept of poseidon: http://www.floatingpowerplant.com/.

[9] (2016). The concept of w2power: http://www.pelagicpower.no/.

[10] (2016). The concept of windsea: http://www.windsea.no/.

[11] Aaron Smith, T. S. and Musial, W. (2015). 2014-2015 offshore wind technologies market report.

[12] Anders Rosen, K. G. (2015). *Naval Architecture Marine Dynamics.*

[13] Anders Yde, Mads Mølgaard Pedersen, S. B. A. K. R. S. C. A. W. N. (2014). Experimental and theoretical analysis of a combined floating wave and wind energy conversation platform.

[14] Bachynski, E. E. (2014). Design and dynamic analysis of tension leg platform wind turbines.

[15] DNV-GL. Wadam user's manual. Technical report.

[16] DNV-GL (2011). *SESAM User Manual HydroD*.

[17] DNV-GL (2016). Sesam user manual: Genie(vol 3 – modelling of plate/shell structures). Technical report.

[18] Greco, M. (2012). Tmr4215: Sea loads lecture notes.

[19] Harald E.Krogstad, A. A. (2000). Linear wave theory part a.

[20] IEC (2005). *International Standard IEC 61400-1: Wind turbines Design requirements*.

[21] J.Jonkman, S.Butterfield, W. (2009). Definition of a 5-mw reference wind tubine for offshore system development. Technical report, National Renewable Energy Laboratory.

[22] J.M.Jonkman, G.J.Hayman, B. R. (2015). Aerodyn v15 user's guide and theory manual. Technical report, National Renewable Energy Laboratory.

[23] Kallesøe., B. S. Wind turbine spacing considerations.

[24] Kenneth Johannessen, Trond Stokka Meling, S. H. (2002). Joint distribution for wind and waves in the northern north sea.

[25] Lee, C.-H. (1995). Wamit theory manual. Technical report, Massachusettes Institute of Technology, Department of Ocean Engineering.

[26] Lee, C.-H. (2008). On the evaluation of quadratic forces on stationary bodies.

[27] Lin Li, Zhen Gao, T. M. (2015). Joint distribution of environmental condition at five european offshore sites for design of combined wind and wave energy devices.

[28] Madjid Karimirad, T. M. (2012). A simplified method for coupled analysis of floating offshore wind turbines.

[29] MARINTEK (2009). Simo theory manual.

[30] Newman, J. (1974). Second order, slowly varying forces on vessels in irregular waves.

[31] O.M.Faltinsen (1999). *Sea Loads On Ship and Offshore Strctures*.

[32] Reza Taghipour, Tristan Perez, T. M. (2008). Hybrid frequency time domain methods for dynamic response analysis of marine structures.

[33] Rhodri James, M. C. R. (2015). Floating offshore wind: Market and technology review.

[34] S.R. Munshi, V.J. Modi, T. (1999). Fluid dynamics of flat plates and rectangualr prisms in the presence of moving surface boundary-layer control.

[35] Veritas, D. N. (2001). Offshroe standard dnv-os-c301: Stability and watertight integrity.

[36] Wang, Q. (2014). Design of a steel pontoon-type semi-submersible floater supporting the dtu 10mw reference turbine. Master's thesis.

[37] Y.H.Bae, M. (2014). Coupled dynamic analysis of multiple wind turbines on a large single floater.

[38] Yttervik, R. (2009). Tdhmill3d user documentation. Technical report, StatoilHydro.